Chapter 8
Zno-Based Dilute Magnetic Semiconductors

Arun Aravind and M. K. Jayaraj

1 Introduction

II–VI-based novel thin films and heterostructures are technologically attractive for future devices due to their exciting electrical and magneto-optical properties [1–3]. The direct band gap ZnO is emerging as a potential candidate due to its ability to tailor electronic, magnetic, and optical properties through doping and alloying [2–6]. ZnO is also an efficient UV emitter. The free-exciton binding energy of ZnO (60 meV) is more than twice that of GaN (25 meV). The radiative recombination in ZnO is mediated by excitons which lead to narrow emission line width. So ZnO-based system has major role in wide range of devices, such as blue and UV light-emitting diodes, spintronic devices based on diluted magnetic semiconductors, transparent conducting transistors, and resonant tunneling devices [2–7].

In II–VI semiconductors, each anion is coordinated by four cations at the corners of a tetrahedron. This tetrahedral coordination is nature of the covalent bond having sp3 hybridization. So the coordinations of Zn^{2+} and O^{2-} are both fourfold. Semiconductors that normally crystallize in wurtzite include nitrides, II–VI semiconductors (ZnS, CdS, ZnSe, CdSe, ZnTe, CdTe, SiC, InAs, etc.). The various forms of crystal structure of ZnO are rock salt or Rochelle salt (B1), zinc blende (B3), and wurtzite (B4); B1, B3, and B4 are designations for the three phases. Wurtzite structure is the most thermodynamically stable phase of ZnO thin films. When it grows on cubic substrates, it shows zinc blende structure, but the rock salt structure is obtained only at high pressures. The wurtzite structure has a hexagonal unit cell with the lattice parameters 'a' and 'c' in the ratio of $c/a = 1.633$ [8]. Under the ordinary preparation

A. Aravind (✉)
Centre for Advanced Functional Materials, Department of Physics, Bishop Moore College, Mavelikara, India
e-mail: bmcarun@gmail.com

M. K. Jayaraj
Cochin University of Science and Technology, Kochi 682022, India

conditions, excess zinc is always found in ZnO. Due to this zinc excess, ZnO is a non-stoichiometric compound and a n-type semiconductor. ZnO is a direct band gap semiconductor (3.37 eV) having an exciton binding energy of 60 meV at room temperature. So ZnO shows near-ultraviolet and the visible defect emissions. The band-edge emission is centered at approximately 380 nm, and the visible deep-level emission is in the range of 450–730 nm. UV emission is the near-band-edge emission which depends on the crystal quality of the film or nanostructures while the visible emissions are related to various intrinsic defects in ZnO crystal [4, 7]. But theses emissions are influenced by growth techniques and conditions.

Diluted magnetic semiconductors (DMS) are semiconductor alloys which contain a small fraction of magnetic impurities. DMSs are mainly based on II–VI materials such as CdTe and ZnSe with transition-metal ions (e.g., Mn, Fe, or Co) substituting the cations. Magnetic ions with +2 valency are easily incorporated into the host II–VI crystals by replacing group II cations of the host lattice. There are also DMS materials based on IV–VI (e.g., PbTe, SnTe) and recently III–V (e.g., GaAs, InSb) crystals, and the rare earth elements (e.g., Eu, Gd, Er) are also used as dopants. In II–VI-based DMS, such as (CdMn)Se, magneto-optic properties were extensively studied and optical isolators were recently fabricated using their large Faraday effect [10]. Recently, ZnO has renewed interest since it was found that high-quality epitaxial thin film shows ultraviolet laser action at room temperature [11, 12]. The band gap of this compound can be extended up to 4 eV by synthesizing alloys of $Zn_{1-x}TM_xO$ (TM = Mn, Co, Ni, etc.). Heavy electron doping was readily achieved in ZnO in contrast to the other II–VI compound semiconductors. According to Ruderman–Kittel–Kasuya–Yosida (RKKY) interaction, the above-mentioned factors favor strong correlation between the magnetic ions and spins of the band carriers of host materials [9, 13–15].

Spintronics is an emerging technology exploiting the intrinsic spin of the electron and its magnetic moment, other than the fundamental electronic charge. Recent past witnessed many advances, particularly in the wide band gap, III–V- and II–VI-based spintronic materials. But practical applications using such materials were limited to low temperature owing to the low Curie temperature (T_C) of the magnetic dopants. Dietl et al. [15] theoretically predicted the possibility of room-temperature ferromagnetism in III–V- and II–VI-based DMS materials. A few transition-metal elements (Mn, Co, Ni, Cu, etc.) that doped ZnO [5, 9, 13–15] exhibits T_C much above 300 K (Fig. 1). TM-doped ZnO is interesting due its room-temperature ferromagnetism and unique transport properties.

Spintronics is becoming an area of active research because it can exploit the spin degree of freedom of the electrons along with its charge. So spintronics can combine standard microelectronics with spin-dependent effects that arise from the interaction between electrons and a magnetic field. So we can expect new generation devices with various functionalities. The magnetic devices should be non-volatile, less electric power consumption, and increased integration densities compared to microelectronics. The discovery of giant magnetoresistance (GMR) [16] in magnetic multilayers has triggered intense experimental as well as theoretical studies to exploit the potential technological applications and to understand the underlying physical phenomena that cause this effect. GMR is realized in metallic multilayers

Fig. 1 Predicted Curie temperature for semiconductors [5, 9]
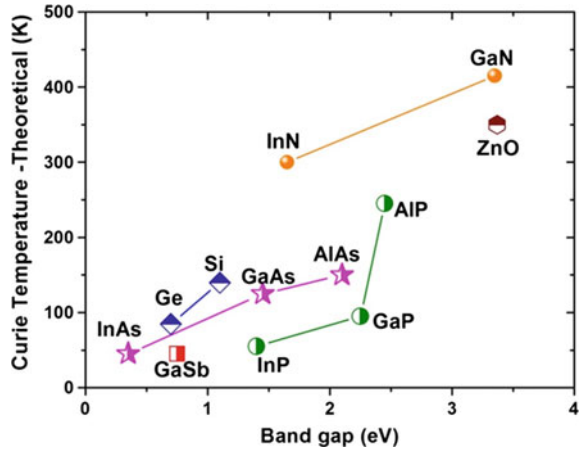
which have alternating layers of ferromagnetic and non-magnetic metallic layers. So in GMR, resistance of the multilayer stack depends on relative orientation of ferromagnetic layers due to spin-dependent scattering at the interfaces. Transition-metal oxide (TMO) is very rich in physics because of unusual magnetic, optical, and electrical properties and has tremendous device applications. Some of the recently discovered applications of TMO are based on superconductors, transparent conducting electronics, optoelectronics, and spintronics [5, 6, 9, 13, 14]. These oxides thin film form have attracted much attention from last decade due to their wide variety of applications such as gas sensors, optical switches, windows for solar cell, thin-film batteries, and photo-catalysis. ZnO is emerging as a potential candidate due to its direct band gap, and also we can tailor the optical and magnetic and properties through doping and alloying [13].

The radiative recombination in ZnO is mediated by excitons which lead to narrow emission line width. So ZnO system has a role for a wide range of devices such as blue and UV light-emitting heterojunction diodes, transparent thin-film transistor for display, and spintronic devices based on diluted magnetic semiconductors. ZnO thin films and nanostructures can be prepared at low temperatures by RF sputtering, pulsed laser deposition, chemical vapor deposition, hydrothermal method, and chemical method [17–21]. Due to ionic nature of ZnO, it lends itself to ease in the microfabrication process using both wet and dry etching techniques. Despite recent experimental success, a fundamental description of ferromagnetism in semiconductors remains incomplete. Recent theoretical treatments have yielded useful insight the possible mechanisms in DMS.

2   Magnetic Interactions in DMS

DMS can be considered as two interacting subsystems, one comprising the host semiconductor with delocalized conduction and valence electrons and the other diluted system of localized magnetic moments associated with the magnetic atoms. The host semiconductors have extended states made by delocalized band electrons. So the optical and electronic properties of DMS are described by the effective mass of the carriers. Magnetic nature of DMS mainly depends on the magnetic moments of the magnetic ions and their interaction with the host semiconductor lattice. Most of them show *sp-d* and *sp-f* interactions for transition-metal ions and rare earth magnetic ions. The spin–spin interaction between magnetic ions can be classified into four major types. RKKY mechanism (Ruderman–Kittel–Kasuya–Yoshida) leads to spin polarization of the conduction electrons of the semiconductors. The band polarization is occurred by Bloembergen–Rowland (BR) interaction [13, 22]. Virtual transition between the magnetic ions and neighboring anions leads to superexchange and double-exchange interactions.

2.1   Carrier-Single Magnetic Interaction

The interaction between the magnetic impurity ion and the conduction and valence band electrons of the host is described by direct Coulomb exchange, i.e., first-order perturbation effect. The direct Coulomb exchange is represented by the ferromagnetic Kondo Hamiltonian [9, 13–15, 22].

$$H_{\text{ex}} = -x N_0 \alpha \langle S_{//} \rangle S_{//}$$

'$x N_0$' is the concentration of magnetic ions with mole fraction 'x', 'α' is the exchange constant for *s* electrons, and $\langle S_{//} \rangle$ is the average magnetic moment along the field direction. $N_0 \alpha$ is the spin exchange integral for conduction band. The value of α is of the about ~0.2 eV for II–VI-based DMS.

2.2   Superexchange Interaction

Superexchange mechanism arises due to the spin-dependent kinetic exchange interaction between each of the two magnetic ions and the valence bands [13, 22]. The four virtual transitions from *p*-like valence band state to the ions and back to the valence band are schematically represented in Fig. 2. When a band electron is transferred to one of these ions, it leads to a hole in the valence band. So the intermediate state is having one magnetic ion with N and second with $N + 1$ electrons. Second

Fig. 2 Schematic representation of four virtual transitions of the superexchange ion–ion interactions [20]
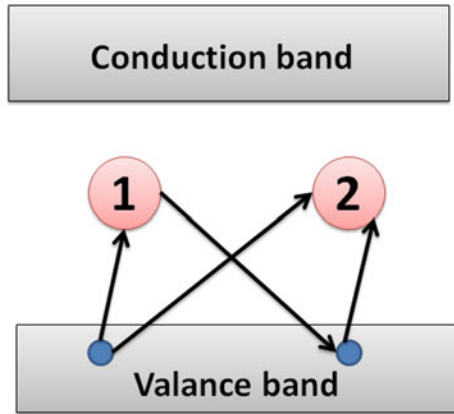
transition arises another possibility with $N + 1$ electron on both ions and two holes in the valence band or one with $N + 1$ and $N - 1$ electrons and no holes in the valence band.

2.3   Double-Exchange Interaction

According to Zener, the double-exchange mechanism is the coupling between the magnetic ions in the different charge states by virtual hopping of the extra electron from one ion to another [13–15, 22]. In Mn^{2+}–Mn^{3+} system, the d-electron will hop between these ions through the p-orbitals.

2.4   RKKY (Ruderman–Kittel–Kasuya–Yoshida) Interaction

RKKY mechanism describes the exchange coupling between the magnetic impurity ion and the band electrons of the host semiconductor lattice. In a degenerated DMS, the interaction is described by s-d Kondo Hamiltonian—first-order perturbation effect [13, 14, 22]. The conduction electron gas gets magnetized by the magnetic ion, and the degree of polarization decreases in an oscillatory fashion with distance from the magnetic ion. This kind of indirect exchange coupling between the magnetic ions may lead to ferromagnetic or antiferromagnetic interaction depending upon the distance of separation of the interacting atoms. The coupling at a distance 'r' having Fermi surface (k_F) is

$$J_{RKKY}(r) \propto \frac{\mathrm{Cos}(2k_F r)}{r^3}$$

2.5 Impurity-Band Exchange and Bound Magnetic Polarons

The ferromagnetic exchange interactions between magnetic moments in n-type DMS are discussed based on its tendency to form shallow donors. Generally, DMS can be represented as $(A_{1-x}M_x)[O\blacksquare]_n$; A non-magnetic cation, M = Magnetic ion, $\blacksquare$ = Donor defects and $n = 1$ or 2. An electron associated with a particular defect will be treated as a hydrogen atom, and the dimension of electron traps is therefore of the order of a few tenths of Å. Consider now the interaction of the magnetic cations M with the hydrogenic electrons in the impurity band. As a result, donors tend to form bound magnetic polarons by coupling the $3d$ moments. The cations present an extra random potential, which extends the localized region of the ions within their orbits [13, 23–26]. Overlap between a hydrogenic electron and the cations within its orbit leads to ferromagnetic exchange coupling between them [25, 26]. This interaction may be written in terms of the s–d exchange parameter J_{s-d} as [13].

$$J_{s-d}S.s|\psi(r)|^2\Omega$$

where S is the spin of the $3d$ cations that have volume Ω, and s is the donor electron spin. Ferromagnetism in DMS arises due to percolation of bound magnetic polarons (Fig. 3). The coupled interaction between localized holes of the polarons and the transition metal producing an effective magnetic field hence aligns the spins. Below the Curie temperature, the neighboring polarons overlap forming clusters of polarons [13, 23–26]. Ferromagnetic transition is possible when the size of the cluster nearly matches the sample size. Despite the low carrier density bound magnetic polarons, the model is applicable to both n-type and p-type host materials.
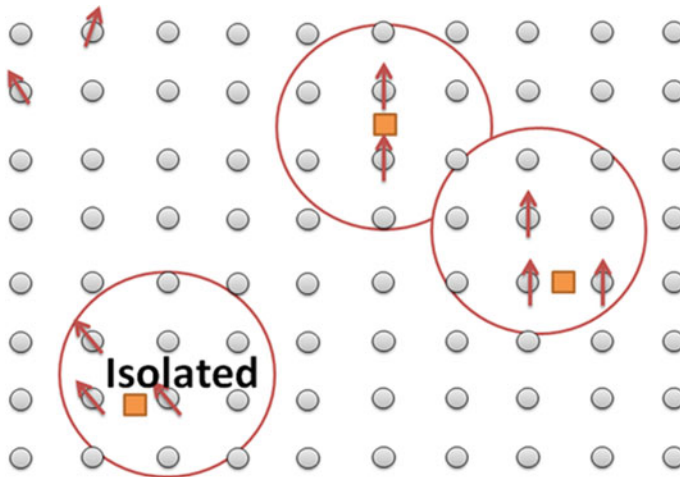

Fig. 3 Schematic representation of magnetic polarons with magnetic cation concentration $x = 0$. Cation sites are represented by small circles [23]

3   Brief Report on TM-Doped Semiconductors

Compared to non-oxide semiconductors, the oxide semiconductors have many advantages. So the wide band gap makes them transparent and also suitable for short-wavelength applications. II–VI group oxides can easily grow at low temperature. So the oxides grow on a plastic substrate and are ecologically safe and durable besides being low in cost. In addition, strong electronegativity of oxygen is expected to produce strong *p-d* exchange coupling between band carriers and localized spins, a prerequisite for DMS [13]. Some of the reports on oxide semiconductor-based DMS are summarized here.

3.1   TiO$_2$-Based DMS

TiO$_2$ has been extensively studied due to its unique properties, like high refractive index, excellent optical transmittance in the visible and near-infrared region, and high dielectric constant. TiO$_2$ crystallizes in three forms—rutile, anatase, and brookite. It has been shown by Matsumoto et al. [27] that the anatase form of TiO$_2$ doped with several percent of Co is ferromagnetic at room temperature. Films of Ti$_{1-x}$Co$_x$ O$_2$ with different x values were made on LaAlO$_3$ (001) and SrTiO$_3$ (001) single crystal substrates. Ferromagnetic long-range ordering was seen in anatase TiO$_2$ doped with 'Co' in the images taken by scanning superconducting quantum interference device (SQUID) microscope. An increase in spontaneous magnetization with the increase in Co content is observed. TiO$_2$ doped with Co shows room-temperature ferromagnetism, with magnetic moment of 0.32 μ_B/Co atom. Matsumoto et al. [27] agree that a possibility of Co clusters cannot be ruled out though XRD and TEM showed no sign of metal granules within the detection limit. In a later article, Matsumoto et al. state that room-temperature ferromagnetism exists in rutile phase of Ti$_{1-x}$Co$_x$O$_2$ with a moment of 1 μ_B/Co atom for 3% Co substitution. Chambers et al. [28] have grown Ti$_{1-x}$Co$_x$O$_2$ films by molecular-beam epitaxy on SrTiO$_3$ substrates having magnetic moment of 1.26 μ_B/Co atom for $x = 0.03$. Chambers et al. [28] also report that the cobalt distribution in their films depends strongly on growth conditions leading to some of their films being non-magnetic. From X-ray absorption spectroscopy measurements, they determine that in the magnetic films the cobalt ions are in the +2 oxidation state and substitute on the Ti site of TiO$_2$. TiO$_2$:Co transparent films grown on both LaAlO$_3$ (001) and SrTiO$_3$ (001) substrates by pulsed laser deposition (PLD) are reported by Stampe et al. [29] which show room temperature ferromagnetism (moment ~ 1.7 μ_B). Cobalt segregation was seen in TEM images. But Kim et al. [30] reported the origin of magnetism by 'Co' nanoclusters in epitaxial TiCoO$_2$ films. Magnetic Circular Dichroism (MCD) studies done on Co-doped anatase TiO$_2$ films also revealed MCD spectral line shape identical to Co metal [30]. Despite all this work, the key question remains to be answered is that if Co is indeed substitution or forms clusters to form ferromagnetic regions within the films?

3.2 SnO$_2$ Materials

SnO$_2$ is semiconductor with rutile structure having octahedral coordination similar to anatase TiO$_2$ [31]. The magnetic measurements revealed almost paramagnetic behavior without any ferromagnetic ordering. A few works were reported on Mn:SnO$_2$. PLD-grown Co-doped SnO$_{2-\delta}$ thin films showed room temperature ferromagnetism [32]. Co content in PLD-grown Sn$_{1-x}$Co$_x$O$_{2-\delta}$ films was higher due to high evaporation rate of Sn. The neighboring magnetic moments of cobalt matrix are unquenched so it shows giant magnetic moments. The origin of giant magnetic moment is still debatable, but the result seems to be promising to explore SnO$_2$-based DMS.

3.3 Importance of TM-Doped ZnO

The strong correlation of '3d' orbitals of transition metals with 's' and 'p' orbitals of the anions can modify electronic structure of ZnO host lattice. ZnO-based DMS gained much attention owing to room-temperature ferromagnetic predictions by Diet et al. [15]. ZnO normally exhibits wurtzite structure, and TM elements have valence electrons in the partially filled d orbitals and in 4s orbitals. TM ions can incorporate into ZnO host lattice contributing its 4s electron to the s-p^3 bonding to give a TM^{2+} state.

Theoretical calculations on ZnO by Sato et al. [33] and Yoshida et al. [34] predicted ferromagnetism at 5% Mn doping without any additional dopants. In order to control electron carrier concentration in Mn-doped ZnO thin films, low-temperature process is preferred [35]. In contradictory [36, 37] to earlier reports, researchers achieved room-temperature ferromagnetism in Mn-doped ZnO [38, 39]. But its reproducibility is still controversial because magnetic properties are very sensitive to thin-film preparation conditions. Pulsed laser deposition has the following advantages such as deposition at relatively high oxygen pressure, high deposition rate, and growth of highly oriented crystalline films at relatively low substrate temperature. ZnO nanostructures were easily grown by hydrothermal and chemical methods. Due to catalyst-free, environmental friendliness, and less hazardous nature, hydrothermal techniques are widely used for large production of nanostructures. The incorporation of Mn^{2+} into hexagonal ZnO lattice even at relatively low temperatures is shown by phase diagram analysis with 13% solubility. Lattice constants of ZnO host lattice changes with increase of Mn content. Similarly, Zn^{2+} shows 10% solubility in MnO at 800 °C [40, 41]. Epitaxial ZnMnO thin films were grown on sapphire substrates at substrate temperatures in the range from 600 to 750 °C. The maximum solubility of Mn in ZnO films is 35%, which is higher than its bulk counterpart. But cobalt-doped ZnO thin films show two magnetic behaviors: a paramagnetic component and a low-field ferromagnetic component. Co-doped ZnO samples grown at high vacuum exhibit ferromagnetism because more oxygen vacancies are inducing free electrons which mediate the ferromagnetic exchange interaction. The formation of cobalt clusters

inhomogeneous film during the growth process favors in ferromagnetism [42]. Optical studies of Co-doped ZnO films show characteristic absorption peaks at 660, 615, and 568 nm. Depending on the growth conditions and preparation techniques, the band gap of Co:ZnO samples shows blue shift or red shift. ZnO films are color less, but $Zn_{1-x}Co_xO$ exhibits light green to dark green color with increase of Co concentration.

Early studies on Cu-doped ZnO system by various groups showed contradiction with each other showing non-magnetic and magnetic nature. Theoretical studies of 25% Cu-doped ZnO system showed non-magnetic behavior but at lower doping levels, 3.125 and 6.25% Cu on ZnO show ferromagnetic nature. Spin-polarized density functional calculations predict that certain ZnO:Cu structures should be ferromagnetic [15]. Under appropriate growth conditions, PLD-grown ZnO:Cu films show ferromagnetism [43]. Jin et al. [44] reported that ferromagnetism was not observed in Cu-doped ZnO thin films prepared by combinatorial laser molecular-beam epitaxy method. Recently, Buchholz et al. [45] reported non-ferromagnetic behavior in n-type Cu-doped ZnO and RTFM in p-type Cu-doped ZnO thin films. Ye et al. [46] theoretically showed that the energy of ferromagnetic state is lower than that of the antiferromagnetic state for Cu-doped ZnO (p-type and n-type) so we can achieve RTFM in this system. According to theoretical modeling, the relative position of copper atoms can strongly affect the magnetic properties of ZnO:Cu system. Some reports show that the stability of ferromagnetism in ZnCuO system depends on the copper atom separation. If copper atoms were separated by 5.20 Å along the c-axis, the ferromagnetic state was favored, but copper atoms were separated by 3.25 Å within the basal plane the antiferromagnetic state was favored. Sato's work looked consistent with other theoretical calculations and together establishing the importance of copper atom placement in the doping process [39]. The metallic copper is not magnetic, and neither Cu_2O nor CuO is ferromagnetic, so ZnO:Cu system is free of ferromagnetic precipitates. Ueda et al. [41] also investigated $Zn_{1-x}TM_xO$ films [n-type ($x = 0.05$–0.25): TM = Co, Mn, Cr, Ni] grown by PLD. The Co-doped ZnO films showed the maximum solubility limit of 30%. In $Zn_{1-x}Co_xO$, only a few films showed ferromagnetic features, while the others showed spin-glass-like behaviors. A few of them exhibited ferromagnetic behaviors with a Curie temperature higher than room temperature with lesser reproducibility. Here also ferromagnetism is directly related to the presence of oxygen vacancies. Detection limits of microstructural characterization will not overrule the possibilities of magnetic impurities like nanosized clusters, substitutional and interstitial impurities over the intrinsic magnetic nature of the thin films [42, 47–49]. In order to determine whether the magnetic atoms substituting into the ZnO host lattice are forming alloys or interstitial defects or impurities, researchers employ X-ray diffraction analysis, transmission electron microscopy, and X-ray absorption studies. It is very difficult to categorize the origin of the ferromagnetism which depends on the level of magnetic dopants. In addition, there are still extreme variations in the reported magnetic behavior with some films exhibiting only paramagnetism and even those with ferromagnetism showing a wide range of apparent Curie temperatures. So the origin of ferromagnetism is till debatable.

Compared to large number of publications on RTFM of Co/Mn-doped ZnO systems, only a few have reported in Ni-doped ZnO systems. But some of them were able to report intrinsic RTFM in Ni-doped ZnO DMS [50–53] or due to Ni clusters [47, 54]. In contradictory to above some reported paramagnetism in Ni-doped ZnO systems [48, 49], ferromagnetism is found only in inhomogeneous films supporting the formation of nickel clusters within the experimental detection limit. Ni:ZnO shows larger magnetism; it cannot be attributed by weak magnetization of nickel oxide. Wakano et al. reported ferromagnetism at 2 K, which becomes superparamagnetism at 30 K and maintain it up to 300 K for Ni:ZnO system [51]. The reported magnetic properties are discrepant, and the origin of ferromagnetism is still controversial.

4 Proposed Spintronic Devices

Spintronic devices came into action after the discovery of the 'giant magnetoresistance (GMR)' in 1988 by French and German physicists [55]. It is due to electron-spin effects in ultrathin 'multilayers' of magnetic materials, their electrical resistance changes with applied magnetic field. In GMR, a non-magnetic metal is sandwiched magnetic metals. The electrical resistance changes from small (parallel magnetizations) to large (antiparallel magnetizations) depending upon the relative magnetic orientations of the magnetic layers. The magnitude of this change is two orders of magnitude larger than is possible with conventional materials, hence the name 'giant magnetoresistance' [16]. IBM found that incorporating GMR materials in read heads would be able to sense much smaller magnetic fields, so hard disk storage capacity can increase from 1 to 20 Gb [56]. IBM launched GMR-based read heads, into the market in 1997. The advantage of magnetic random access memory (MRAM) is that it is 'non-volatile'—information is not lost when the system is switched off but it can be smaller and faster. MRAM devices use less power and would be much more robust in extreme conditions such as high temperature or high-level radiation or interference.

4.1 Overview of Spin-Based Devices and Its Applications

The realization of spintronic devices depends how we can create and control spin-polarized charge carriers in our existing semiconductors. This can be accomplished by optical pumping using appropriately polarized laser light. The working of spintronic devices outlined as: (1) information is stored into the particular spin orientations of spins (up or down), (2) it is attached to mobile electrons for carrying the information along a wire (3), and the information is read at the output terminal [21]. Spintronic devices are attractive for memory storage and magnetic sensor applications. Due to larger coherence length, it is a potential candidate for quantum computing where electron spin would represent information as qubit [17].

Semiconductor-based spintronic devices like to add the unique features of magnetic devices to our conventional electronic devices like field-effect transistors and light-emitting diodes [16, 57]. So the memory and microprocessor functions can be integrated into the same chip. The successful realization of most spintronic application depends critically on the ability to create spin-polarized charge carriers in a conventional semiconductor device. So the spin-polarized carriers can be injected from a spin-polarized source or effective spin-filtering at the interfaces. The spin injection from a conventional ferromagnetic metal into a semiconductor is highly inefficient than other methods. Using spin-polarized dilute magnetic semiconductor as our injector or by paramagnetic semiconductors at high magnetic field as a spin filter, we can successfully demonstrate spin injection in semiconductor tunnel diodes.

The most effective measurement of the quality of the oxide-based ferromagnetic materials will be in the operation of device structures, such as spin-field-effect transistors (FET) (Fig. 4), or photo-induced ferromagnets. Using ferromagnetic semiconductors as the injection source, one should directly measure the efficiency and spin transport length. ZnO-based test structure will exploit or demonstrate the novel aspects of ferromagnetism in the devices. (Zn, Mn)O is showing antiferromagnetic spin-glass-like insulating behavior, and Mn-Co-doped ZnO is having half-metallic ferromagnetic nature. The negative gate bias brings holes into (Zn, Mn)O, and it can be converted to half-metallic ferromagnetic state. Using ferromagnetic (Zn, Co)O as the source and drain contact material, it should be possible to have a 100% spin-polarized electron flow in the (Zn, Mn)O channel. Spin FET can be fabricated by growing source and drain on top of (Zn, Mn)O layer and etching away the selective region for the growth of gate oxide and deposition of the gate metal.
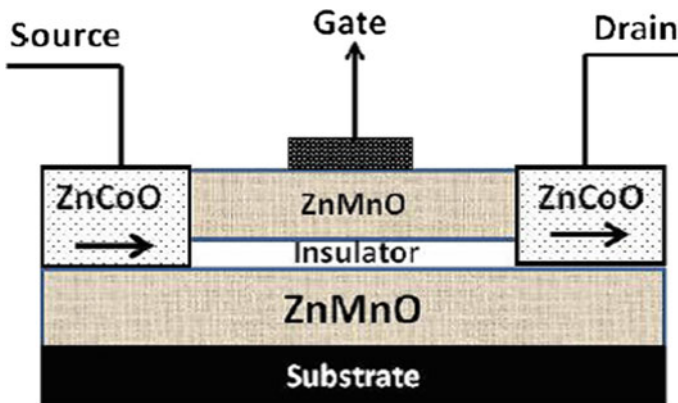

Fig. 4 Spin FET—single transistor non-volatile memory [6, 16, 57]

4.2   *Co-Doped ZnO-Based Magnetic Tunnel Junctions*

In order to study the effect of spin injection and spin polarized transports in spin-tronic devices TM doped ZnO based heterostructures have been developed [6, 16]. (Zn, Co)O used for fabrication of two FM electrodes and insulating ZnO layer as the barrier, because it allows the epitaxial growth of (Zn, Co)O layer [16, 57]. (Zn, Co)O/ZnO/(Zn, Co)O epitaxial structures (Fig. 5) satisfy two primary requirements for spin injection: a minimum conductance mismatch and high spin-polarized contacts [58]. Tunnel magnetoresistance (TMR) is expected to persist up to RT (room temperature) and exhibit high $V_{1/2}$ to overcome one of the main shortcomings of magnetic tunnel junctions (MTJs). In order to study the effect of spin injection and spin polarized transports in spintronic devices TM doped ZnO based heterostructure have been developed [6, 16] (Fig. 6).

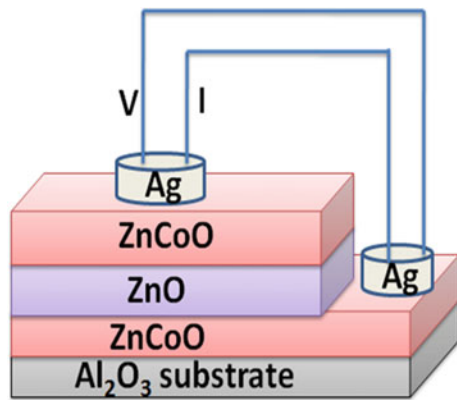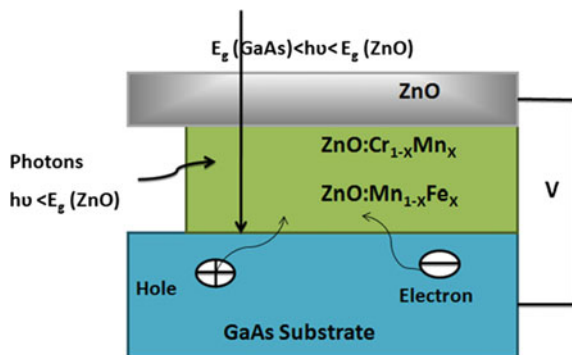**Fig. 5** Schematic representation of a (Zn,Co)O/ZnO/(Zn,Co)O junction [6, 16]

**Fig. 6** Schematic of ZnO-based transparent photomagnet [57]

5 Theoretical and Experimental Hurdles in the Realization of RTFM in TMOs

A lack of stability and reproducibility prevents definitive conclusions from being drawn from much of the data on high-temperature ferromagnetism. It is often difficult to recover the same magnetic behavior in different laboratories or even within the same laboratory at different times. Furthermore, the ferromagnetic signals frequently prove to be transient, decaying in time over periods of days or months. Recent work on spintronic focuses on achieving higher transition temperature magnetic materials for technological applications. While the progress in synthesizing and controlling magnetic properties of group III-arsenide compound semiconductors has been astounding, the reported Curie temperatures are too low (~172 K) [15, 59] to have a significant practical impact. A key development that focused on wide band gap semiconductors as being the most promising for achieving high Curie temperatures was the work of Dietl et al. [24]. According to Zener model of ferromagnetism, they predict T_C values for several materials. The schematic diagram (Fig. 7) showing the predicted T_C values is given below [5, 15].

Carrier-mediated ferromagnetism on DMS depends on the nature of magnetic dopants carrier type, concentration and carrier density. When these systems approaching metal–insulator transition, carrier density is increased as result ferromagnetism is observed. They observed a gradual progression from localized states to itinerant electronic states as the carrier density increases. During metallic transition, the population density of some of the electrons can be extended while others can occupy the impurity states. The extended states become localized while crossing the metal–insulator boundary, and as a result, the localization radius decreases gradually. For interactions on a lengthy scale smaller than the localization length, the electron wave function remains extended. The long-range interactions between localized spins are

Fig. 7 Experimental prediction of ferromagnetism in various semiconductors [5]
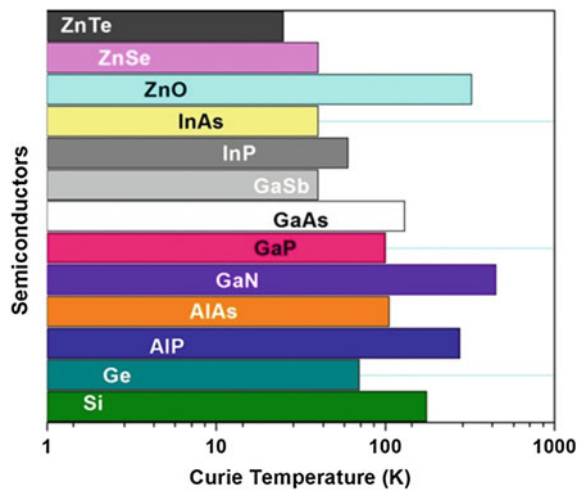
possible due to holes in extended or weakly localized states. So the carrier-mediated ferromagnetic interactions may be possible for heavily doped semiconducting oxides. A lot of studies were on the electronic structure of the ZnO-based TMOs, and their interactions are done based on ab initio calculations or first principle studies [59–67].

(a) **Electronic structures of (Zn,TM)O (TM: V, Cr, Mn, Fe, Co, and Ni) in the self-interaction-corrected calculations**

Origin of magnetism in DMS is always a debatable one, so the electronic studies are a field of interest for the theoretical physicists' in DMS. Fukumura et al. [40] successfully grown Zn(Mn)O, after that a large number of experiments on ZnO-based DMS have been conducted by various groups across the world. But there is a markable discrepancy in the magnetic ground state and magnetic moments. Sometimes secondary phases or even nanoclusters were responsible for the experimental observable magnetic behavior in DMS. So one must be well aware of the growth parameters and the artifacts rose during structural and optical characterizations. Sometimes the observed ferromagnetism is mediated by holes in the valence band or by conduction electrons so the electric natures, oxidation states of the DMS are studied thoroughly. So the theoretical works like first principle studies have come into play. Toyoda et al. [65] calculated the electronic structures of ZnO-based dilute magnetic semiconductors within the self-interaction-corrected local density approximation (LDA). Their results are good agreement with earlier data calculated using standard local density approximation theory. We found that there are differences in the band gap energy, the energetic position of the Zn 3d bands, and the description of the transition-metal d bands [64–66].

The presence of self-interaction is the main short comings of LDA studies. So Toyoda et al. [65] carried out the calculations on ZnO-based DMS by using a self-interaction-corrected LDA approach. They also presented the systematic comparison of the electronic structures of ZnO-based DMS calculated within the self-interaction-corrected LDA and the standard LDA. The transition-metal 3d bands change more drastically, and a chemical trend is seen in the shapes of partial density of states (DOS) of those. In (Zn, V)O and (Zn, Cr)O, the 3d bands shift downward in energy by 1 eV, but still appear within the band gap as they are in LDA. According to standard LDA studies, the transition-metal d-density of states at the Fermi level plays an essential role for getting the ferromagnetic ordering in the ZnO-based DMS. The ferromagnetic ground state is stabilized through the double-exchange interaction and hopping of d-electrons. Extensive studies were done on (Zn, Co)O after the observation of room temperature ferromagnetism [68–71]. In LDA, the Fermi level lies in the gap of the tetrahedral-like crystal field splitting of the d-states, but due to the band broadening, d-density of states exists at the Fermi level. Compared to those calculated within the standard LDA (1), the larger band gap energy, (2) the Zn 3d bands are correctly separated from the valence band (3), and the qualitatively different descriptions of the transition-metal 3d states are obtained. These features, especially the description of the transition-metal 3d states, could affect the predicted magnetic properties [60, 64–66]. The researchers believed that in order to get useful

devices, we need to have single-phase dilute magnetic oxides, because the spin-polarized charger carriers transform the spin information. But multi-phase materials also found applications in magneto-optical devices.

The wide band gap semiconductor-based spintronic applications need the coupling between the ferromagnetism and the semiconducting properties. As initial results, at room temperature, ferromagnetic oxides were obtained in anatase and rutile-type TiO_2:Co [27–30]. Ferromagnetism in magnetically doped ZnO has been both predicted [5, 15] and observed [6–8, 23, 40, 41, 59–61, 68–71]. In addition to Mn doping and additional charge carriers, the ferromagnetic ordering occurs when the magnetic indirect exchange interaction is mediated by hole though the host valence band. This is also suggested to occur for Cr, Fe, Co, and Ni dopants [61]. The key aspect of Pearton et al. [60] work is to achieve soluble concentrations of the transition-metal ions well above their equilibrium solubility limit. In order to achieve this, we have to use non-equilibrium methods such as low-temperature epitaxy or ion implantation. In the remainder of this review, the detailed results for specific combinations of hosts and transition-metal ions will be discussed. Ferromagnetism appears in degenerated or non-degenerated semiconductors and in insulators, if the concentrations of $3d$ dopants are less than the threshold value required for nearest-neighbor cation coupling. The average moment per dopants cation approaches (or even exceeds) the spin-only moment at low dopants concentrations (x), and it falls progressively with increase of dopant concentration (x_p). Superexchange interaction, which is predominantly antiferromagnetic and short-ranged [13, 23], cannot be invoked because the magnetic order appears at concentrations of magnetic cations $x < x_p$. The ferromagnetic double-exchange mechanism, as described by Zener with reference to mixed-valence manganites, can produce large moments, but it is also a nearest-neighbor interaction that requires mixed cation valence, so that $3d_n \leftrightarrow 3d_{n+1}$ configuration fluctuations can occur. There is no evidence that mixed valence is a common feature of these dilute oxides. Longer-range ferromagnetic exchange can be mediated by carriers in a spin-polarized band.

A large number of reports on TM-doped ZnO DMS have been published during the last decade. Literately, a few research works were on V-, Cr-, Ti-doped ZnO-based DMSs compared to Co and Mn dopants [6, 38–44, 68, 72–75]. According to literature reviews, ZnO films doped with 5 at.% Co commonly exhibit much stronger RTFM than ZnO doped with other TM elements, because Co is more soluble in ZnO host lattice [6, 41–44, 68]. Room-temperature magnetic moments reported for 5 at.% TM-doped ZnO films are summarized in Fig. 8. In terms of concentration-dependent magnetization, the largest moments have been observed for ZnO doped with different TM concentrations, i.e., 2–5 at.% for Co [6, 41–44, 68, 76], 2 at.% for Mn [6, 38–41, 72–75], and 1 at.% for Ni and Cu [6, 40–44, 77]. According to these studies, ZnO films with higher dopants contents tend to show much lower magnetic moments. Therefore, besides ideal moment discrepancies for these TM ions in ZnO films, different solubility and different maximum dopants' concentration would also account for different magnetic moments in 5 at.% TM-doped ZnO films (Fig. 8).

Fig. 8 Plots of magnetic moment per transition-metal cation (5 at.%) doped in ZnO thin films [6]
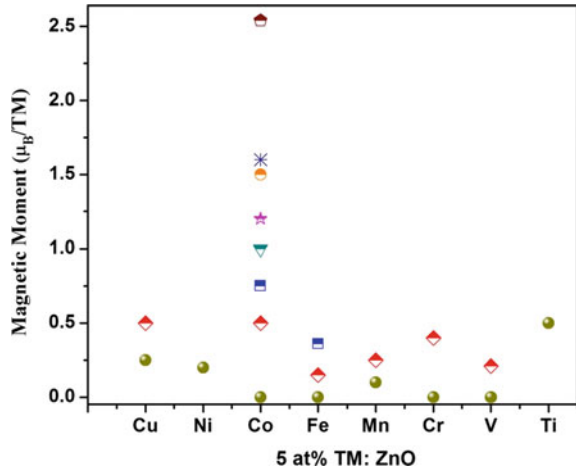
5.1 Experimental Limitations in Magnetic Measurements

Modern solid-state physics make use of sensitive magnetometry an essential tool to study the magnetic properties in ultrathin films and nanostructures. Recent developments and intensive magnetic measurements in the field of colossal magnetoresistance (CMR), tunneling magnetoresistance (TMR), anisotropic ferromagnetism, etc., pave way to studies which discuss the influence of artifacts in improper sample handling and residual magnetic signals in SQUID magnetometer. The magnetic measurements of thin films and powder samples are performed using Quantum Design SQUID magnetometer MPMS (XL). The wide acceptance of MPMS-SQUID is mainly due to its high degree of user-friendly automation and reliability, as well as the lack of commercial alternatives. SQUID magnetometer is one of the most sensitive experimental techniques used for high-sensitivity magnetic characterizations. But in practice, especially for thin-film samples, the magnetic signal recorded with a commercial MPMS-SQUID magnetometer is dominated by artifacts below 0.5×10^{-6} emu.

(a) **Artifices due to improper sample handling**

Normally, the precise magnetic measurements have been taken with an MPMS XL (5T) MPMS (XL) by Quantum Design [78, 79]. For all measurements, the reciprocating sample option (RSO) of the MPMS was used which offers a higher sensitivity than the standard DC transport. In Quantum Design SQUID magnetometer, we use drinking straw as the sample holder. Most of the researchers exclusively use the unit emu in their magnetic measurements. During low signal measurements, the absolute size of the overall signal determines how close magnetic signals are to artifact-level of the instruments.

In order to point out the magnetic anomalies due to improper sample, Ney et al. [79] have studied the hysteresis measurements of sapphire after cleaving. The raw

data show a clear discontinuity of the signal after passing the zero value. The step-like behavior with saturation magnetization is obtained after the subtraction of the diamagnetic background. The corresponding x-position of the measured magnetic moment is plotted. A big step is correlated with the kinks in the hysteresis curves [79]. Finally, the same sample was measured after intensive cleaning which demonstrates that the previous signal may from ferromagnetic contaminations due to improper sample handling. The signature of x-position is typical for edge contamination. During a measurement, the sample is moved along the pickup coils while the respective voltage is recorded. SQUID magnetometer uses fitting routine to correlate the amplitude and position of the signal from the sample to overview the possible shifts due to temperature or positional changes during the measurements.

Other kinds of artifacts occur when magnetic measurements on the non-homogeneous ferromagnetic sample on diamagnetic substrates are performed, viz. nanoparticles grown on substrate, magnetic ions implanted on thin films, or uneven distribution in samples prepared by lithography. Due to cleaving of the samples into suitable dimensions, the tendency of magnetic contamination at the edge also increases. Normally, we use a diamond stencil for cleaving in which a tiny piece of diamond attached to a stainless-steel rod. If this rod touches the edge of a very hard substrate material like sapphire or carbides, the chances of small particles of the metal which get abraded are very high. So we need a thorough cleaning of the substrates especially if sapphire or single crystals are used for thin-film deposition. In case of softer substrates, the situation is less critical because the cleaving does not produce any detectable ferromagnetic contaminations. It is better practice to use plastic or non-contaminative tweezers for sample handling to avoid unintentional magnetic contamination during film preparation and transferring it to SQUID system.

(b) **Artifices from the SQUID system**

SQUID itself will give artifacts which may lead to pick up wrong magnetic signals from samples other due its improper handling. In MPMS-SQUID, the actual magnetic field is merely determined by the voltage drop over a shunt resistor. The magnetic field of the magnetometer is measured by the voltage drop over two shunt resistors which account for different field ranges. So this magnetic field control has to be well calibrated on a regular basis using the manual from Quantum Design. In order to operate in wide field range of the MPMS, the instruments have two shunt resistors with respective amplifiers, both of which have to be calibrated to avoid discrepancies in the applied magnetic field. But a very careful calibration of both detection channels usually results more or less 1% of discrepancy between the actual magnetic fields in the two modes. The second calibration concerns the zero-current offset of the regulated power supply arrangement in the MPMS. Sometimes the FC/ZFC (field cooled/zero field cooled) measurements exhibit a negative magnetization after the diamagnetic background for the nominal field value of 10 mT has been subtracted [78, 79]. The magnetic field control of the SQUID can cause offset fields which lead to inverted hysteresis curves or FC/ZFC curves with negative magnetization values (even though a positive measuring field is applied). A residual misfit of about 1% remains typically and can cause artifacts at about 350 mT.

During the small signal measurements of DMS, the diamagnetic signal of the substrate dominates the weak ferromagnetic or superparamagnetic magnetic response at high magnetic fields. Typical substrate sizes lead to a diamagnetic response of the order of 10^4 emu at higher magnetic fields. Sometimes the real signal from the thin film is very small, but the total signal becomes larger with increasing magnetic field due to diamagnetic contributions from the substrate. Such a dynamic range can be accessed 'autoranging' option where the sensitivity range is selected automatically. In this mode, MPMS will adjust two different factors, which are termed 'gain' and 'range'. 'Gain' simply changes the gain of the voltmeter card by a multiplication factor. The 'range' refers the time constant of rf-amplifier integrator in the rf-SQUID. When there is a clear change in slope of the measured data, then the shunt resistors have to be re-calibrated for realistic data. So these kinds of artifacts are removed by subtracting a different diamagnetic background which is account for the different magnetic field scale.

(c) **Residual magnetic signals**

Normally, the magnetic measurement of crystals or thin films at different temperatures shows hysteresis loop, but it reveals a paramagnetic signal at low temperatures and high magnetic fields. The reduction of coercivity at low temperature is due to superimposition of paramagnetic contribution from the sample. The absence of a true ferromagnetic signal is inferred by the FC/ZFC curves which are not separated at any temperature. The residual magnetic signals also create artifacts during magnetic measurement sequences. The residual hysteresis can be attributed to residual magnetic flux trapped in the superconducting magnet. The residual magnetic flux is independent of the charging state, and it adds to the magnetic field but aligns with the direction of the overall field. So if one should use the magnet reset option during a sequence, we can detect very small residual signals.

The artifacts and limitations of a commercial MPMS-SQUID magnetometer demonstrate that the hysteresis measurements are only a necessary but not a sufficient criterion to prove the existence of ferromagnetism if the size of the signal is small. But the artifacts from contaminated cleave edges of the sample or misaligned magnetic field controls are easily ruled out. Although MPMS is a very versatile and convenient magnetometer but when a thin film on a substrate is inserted, imperfections of the sample mounting, size effects, possible contaminations, and especially the overall diamagnetic background of any used substrate make reliable detection of signals up to 0.5×10^{-6} emu.

5.2 *Effect of Growth Parameters*

Most of the reports and recent reviews are mainly focused on the enhancement of magnetic behavior of II–VI oxides and its dependence on preparation conditions such as the doping concentration, substrate temperature, and oxygen partial pressure [6, 9, 23–25, 42, 59–61, 68, 80, 81]. A few of them have directly investigated the

substrate-dependent magnetic behavior, substrate orientation and substrate temperature, deposition rate, etc. [6, 80–82]. In reality, most groups have focused on doping concentrations below the solubility limit to obtain true DMS. The different groups show distinct magnetic behaviors owing to the effects of the preparation method and growth parameters. So it is worth to evaluate the effect of dopants' concentrations on magnetization from a series of experiments.

(a)   **Effect of substrates**

The most commonly used substrates for ZnO:TM thin films depositions are quartz [6, 72–74, 82, 83], Si [6, 84–88], Al_2O_3 [6, 42, 89–92], and ZnO [93–95]. The local structure and magnetization of ZnO:TM have direct dependence on experimental conditions, the preparation method, oxygen partial pressure, substrate temperature, etc. However, ZnO:TM films deposited on different substrates with the same deposition parameters show distinct magnetization. Sudakar et al. [96] showed that Cu (6 at.%)-doped ZnO films on quartz and sapphire substrates exhibit 1.6 and 1.2 μ_B/Cu magnetization at 300 K. Similarly, RTFM with a magnetic moment of 1.5 μ_B/Co atom was observed for $Zn_{0.95}Co_{0.05}O$ films deposited on ZnO substrate, but only weak FM signals were detected for films grown on Al_2O_3 [97]. This difference can be explained by different structural properties, and defect densities in the films arise due to difference in the crystalline nature of the substrates [6, 42, 68, 80, 81, 95–97]. Thus, it seems that the substrate most likely impacts the local 'TM' structure and magnetization of TM-doped ZnO due to defects in the film or at the boundaries. The magnetic moment of ZnO:Co thin film varies as 0.62, 0.66, and 0.24 μ_B/Co for films deposited on Al_2O_3, Si, and NaCl single crystal, respectively. So it is clear that crystalline nature of substrate has a direct influence on the magnetic behavior of Co-doped ZnO films. ZnO:Co thin films deposited on glass substrate does not exhibit any RTFM [82]. Normally, the diamagnetic background of the substrate has been subtracted from all of the magnetization data, indicating that the difference in moments in ZnO:Co films does not arise from the substrate. It is worth pointing out that reorganization of the defects could partly occur due to the comparatively weak polarization of the SiO_2 piezoelectric substrate, leading to a lower moment per Co atom in Co-doped ZnO film, e.g., 1.1 μ_B/Co. Although the Co dopant exists in a '+2' state when substituting for Zn^{2+}, randomly distributed defects would lead to very weak moments or no RTFM in Co-doped ZnO films on other single substrates (e.g., Al_2O_3, Si, and NaCl) and glass substrate, respectively [82]. $Zn_{0.962}Co_{0.038}O$ films deposited on $LiTaO_3$(1 1 0), (0 1 2) and (0 1 8) substrates by DC reactive magnetron co-sputtering exhibited different magnetization of 1.21, 2.42, 0.65 μ_B/Co, respectively. It is likely that the magnetization differences for Co-doped ZnO films on three oriented $LiTaO_3$ substrates can be attributed to the film microstructure and the Co–O bond length, which primarily depends on mismatch between the film and the different oriented substrates [6, 95–98]. Some of the works on Co-doped ZnO thin films show that the boundary between film and substrate is the defect formation region which in turn affects the magnetization [6, 60, 68, 82, 95–98]. According to a large volume of reviews and repots, we can easily conclude that the substrate, its

crystalline nature, and orientation strongly affect the magnetization of TM-doped ZnO films to certain extents.

(b) **Influence of post-annealing and formation of secondary phases**

Annealing has a direct impact on the microstructure of the thin films with reduction or enhancement of defects with respect to the annealing atmosphere. Some of the experimental results of ZnO:TM systems on annealing demonstrate that magnetism have direct dependence on intrinsic defects like vacancy of oxygen V_O and zinc interstitial Zn_i. Normally, the magnetization of ZnO:TM thin films or nanocrystals annealed in vacuum or a reducing atmosphere should be enhanced [6, 60, 68, 74, 77, 83, 86, 89, 92, 99–108]. It is mainly due to the introduction of V_O [6, 68, 74, 83, 89, 92, 100, 103, 105] or Zn_i, which are critical for RTFM in TM-doped ZnO [6, 68, 86, 92, 101, 105, 107, 109]. The free electrons of the host are locally trapped by these defects which occupy an orbital overlapping with the 'd' shells of TM neighbors to form a bound magnetic polaron(BMP), which in turn accounts for the intrinsic RTFM in DMS. Annealing of Co-doped ZnO films in air and Zn vapor atmosphere, Kittilstved et al. [107] demonstrated reversible cycling of saturated magnetic moments in ZnO:Co thin films. The microstructure and magnetic properties of $Zn_{0.92}Co_{0.08}O$ films annealed at different temperatures (200, 400, and 600 °C) in vacuum and air were systematically investigated by Liu et al. [105]. At same annealing temperature, the magnetic moment increased at vacuum and decreased at ambient air conditions. The vacuum-annealed film shows saturation magnetization (M_S) of approximately 0.45 μ_B/Co, which is slightly greater than for the as-grown film (0.34 μ_B/Co), whereas the value for the air-annealed film (0.21 μ_B/Co) is much lower than Ms of the as-grown film. But annealing at higher temperature normally improves the crystal quality and a corresponding decrease in structural defects in the film as a result the defect mediated magnetism also reduces. On the other hand, annealing in air at high temperature ($\geq$600 °C) TM^{2+} ions may segregate from the crystal and form secondary impurity phases or metal precipitates, which will reduce the RTFM. So we can conclude that low temperature and reducing atmosphere favor the defects formation and enhance FM ordering.

(c) **Comparison of experimental works on ZnO doped with TMs**

A large number of reports on TM-doped ZnO have been published in the last decade. Most of the research groups mainly focus on Co- [6, 41, 68, 82, 83, 92, 98, 105, 107, 110] and Mn-doped ZnO films [6, 38–41, 72–75]. The dopants used to attain room-temperature ferromagnetism in ZnO are shown in Fig. 9. Transition-metal ions show different thermal solubility in ZnO host lattice. Co and Mn show much higher thermal solubility limits than those of Ti, V, Cr, Fe, Ni, and Cu [6, 41–44, 68]. ZnO films doped with 5 at.% TM commonly exhibit much stronger RTFM than ZnO doped with other TM elements. This is consistent with results obtained by Ueda et al. [41] and Venkatesan et al. [110] for ZnO doped with a series of TM elements; such studies can exclude the influence of the preparation parameters on magnetic ordering. It is evident that ZnO films doped with different TMs exhibit RTFM with different M_S values, as well as very small magnetic moments indicating negligible
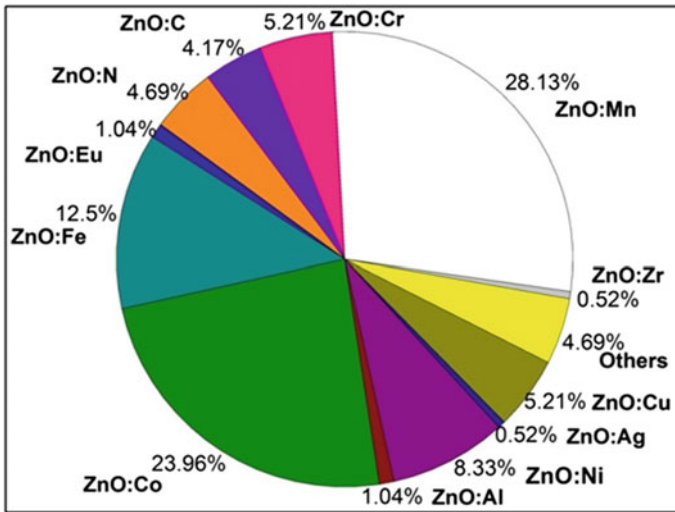
Fig. 9 Pie chart of ZnO-based DMS with different TM dopants [6, 41–44]

FM. Normally, the TM-doped ZnO films are either conducting or semiconducting, as characterized by strong coupling between localized d-electrons of the TM ions and the extended s and p carriers of ZnO. So we can spin-polarize the carriers as a result FM ordering of magnetic moments of TM ions can maintained in the oxide lattice. Some groups showed RTFM with an inverse correlation between magnetization and electron density. So the intrinsic RTFM of TM-doped ZnO systems always remains an open question for the research community.

(d) **Effect of co-doping in magnetic properties**

As per above discussions, earlier works show that the RTFM in ZnO:TM can be enhanced by the increase of the carrier concentration by controlling the experimental parameters like decrease of deposition pressure, low-temperature deposition, post-annealing, etc. In contradiction to this, some researchers have reported that the creation of free carriers is not a sufficient condition for RTFM [73, 76]. Some groups also reported the RTFM in the absence of free carriers [6, 23, 80, 90, 111–115]. If the carrier concentration can enhance RTFM or there is a relation between them, researches use co-doping to generate additional electrons/holes. ZnO is intrinsically n-type semiconductor [89, 93, 116–120], whereas N, Li, and Cu are used for hole doping [119, 121–124]. So these studies show that the increase of carrier concentrations by additional dopants can enhance the RTEM. Ivill et al. [117] designed a series of experiments on (Mn, Sn)-Co-doped ZnO with varying Sn concentration (0–0.1 at.%). But they found an inverse correlation between magnetization and electron density, as a function of the Sn doping. This phenomenon is most consistent with the bound magnetic polaron (BMP) model in which bound acceptors mediate FM doping. RTFM arises with increase of donor defects or electron carrier concentrations,

but these two factors coexist in most doped ZnO systems and are hard to distinguish. Similarly, Al doping in the $Zn_{0.95}Co_{0.05}O$ thin film, implying a decrease in crystalline quality and an increase in structural defects on inclusion of a trace amount of Al [119], in turn enhances the magnetic moment per Co ion of ZnO:Co films. Normally, the co-dopants could trigger other defects, which in turn enhance the FM but the concentration of the co-dopants plays crucial role. Ueda et al. [41] showed that ZnO:Co system exhibits ferromagnetic nature above 280 K for 5–25% Co and 1% Al, without any secondary phases or clusters. After the theoretical predictions [1–3, 5–7, 14, 15], most of experimental works have proved the existence of room temperature ferromagnetism in Mn, Co, Ni, and Cu-doped ZnO, but the nature and origin of room temperature ferromagnetism (RTFM) is still debatable.

5.3 Growth and Characterization of PLD-Grown ZnO:TM Thin Films

$Zn_{1-x}TM_xO$ thin films (TM: Mn/Co/Ni/Cu) were grown on fused silica substrates by pulsed laser deposition (PLD) technique. The fourth harmonic of Nd:YAG laser (266 nm) with repetition rate of 10 Hz and pulse width 6–7 ns was used for ablation. The ablation was carried out at laser energy density of 1.1 J cm^{-2}. $Zn_{1-x}TM_xO$ thin films with various TM concentrations were grown at different substrate temperature (350–650 °C) and oxygen pressure 0.05–5 × 10^{-4} mbar. The deposition duration was 1 h resulting a film thickness ~200 nm. XRD pattern of TM-doped ZnO and pure ZnO thin films deposited at 450 °C on fused silica substrate show the characteristic peak of ZnO corresponding to the wurtzite structure of the ZnO. No trace of secondary phases or binary zinc transition-metal phase is observed within the detection limit of XRD.

The colors of $Zn_{0.95}Mn_{0.05}O$, $Zn_{0.95}Co_{0.05}O$, $Zn_{0.95}Ni_{0.05}O$, and $Zn_{0.95}Cu_{0.05}O$ film becomes, respectively, yellowish, greenish blue, light green, and light blue with the incorporation of TMs. Ni- and Co-doped ZnO shows predominant visible d-d transitions in the tetrahedral geometry (Fig. 10). The Co have absorption around 1.89, 2.03 and 2.19 eV corresponding to $^4A_2(F) \rightarrow {}^2A_1(G)$, $^4A_2(F) \rightarrow {}^4T_1(P)$ and $^4A_2(F) \rightarrow {}^2E_1(G)$ d-d transitions respectively which are in agreement with the one observed in Co^{2+}. The Ni-doped ZnO thin films show absorptions around 2.10, 2.26, and 2.39 eV, the corresponding d-d transitions $^3A_2(G) \rightarrow {}^3T_2 (G)$, $^3A_2(G) \rightarrow {}^3T_1 (G)$, and $^3A_2(G) \rightarrow {}^3T_1 (P)$. The band gap of $Zn_{1-x}Mn_xO$ and $Zn_{1-x}Co_xO$ thin films shows blue shift, while $Zn_{1-x}Cu_xO$ and $Zn_{1-x}Ni_xO$ shows red shift compared to pristine ZnO. The Burstein–Moss effect and sp-d exchange interaction are responsible for the observed blue and red shift in the TM-doped ZnO thin films. The s-d and p-d exchange interactions will give negative and positive corrections to conduction band and valence band of the host semiconductors, and it leads to band shrinking [33]. In heavily doped semiconductors, the donor electrons occupy the bottom of the conduction band, and it will in turn block the low energy transitions, which provide

Fig. 10 Transmission spectra of $Zn_{1-x}TM_xO$ films for $x = 0.05$
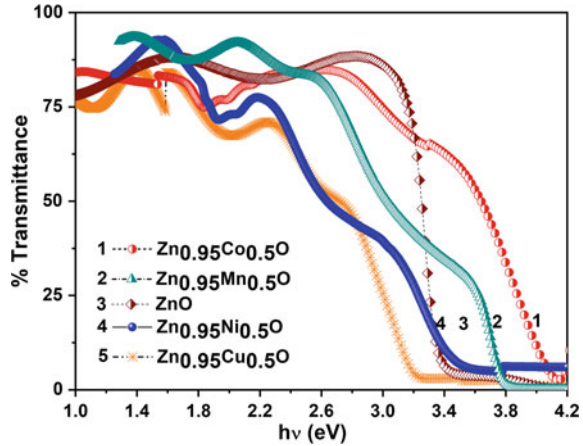
the band gap widening and is known as Burstein–Moss shift [125]. The character of the band gap becomes more indirect with the addition of Co/Mn. The increase of carrier concatenation in Mn- and Co-doped ZnO thin films was confirmed by Hall measurements.

Raman scattering is one of the effective techniques to investigate the crystallization, structure, and defects in the thin films. The non-polar E_2 modes of ZnO have two frequencies, namely E_2^{high} and E_2^{low}, associated with the motion of oxygen atoms along with zinc. The Raman spectra of the $Zn_{0.95}TM_{0.05}O$ thin films (Fig. 11) show three predominant modes at (99 cm^{-1}), E_2^{low}, (435 cm^{-1}) E_2^{high}, and $E_1^{LO}(585 \text{ cm}^{-1})$. All the $Zn_{1-x}TM_xO$ films have spectra similar to ZnO, indicating that the wurtzite structure is not changed with the TM doping [126–130]. The boarding of the E_2^{high} modes and its red shift indicates the substitution of TM into the ZnO sublattice [129–134].

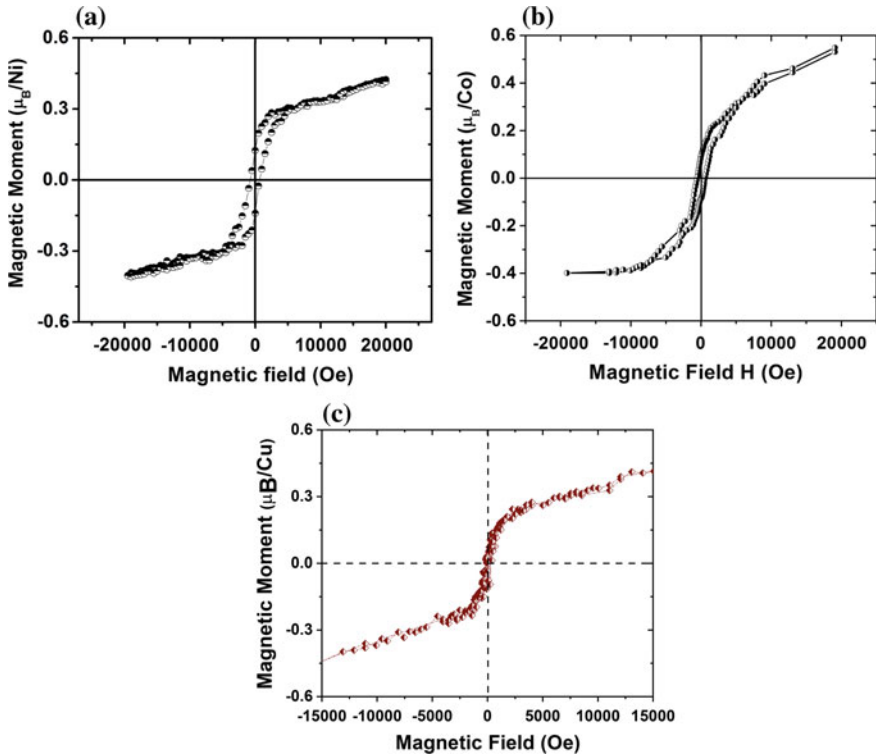**Fig. 11** Room-temperature Raman spectra of $Zn_{0.95}TM_{0.05}O$ films (TM = Mn/Co/Ni/Cu)
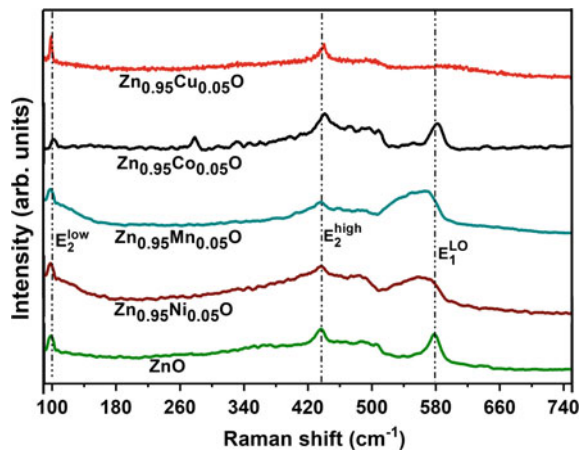
Fig. 12 Room-temperature M-H curve of **a** $Zn_{0.97}Ni_{0.03}O$, **b** $Zn_{0.95}Co_{0.05}O$ and **c** $Zn_{0.97}Cu_{0.03}O$ films

M-H curve of the $Zn_{0.97}Ni_{0.03}O$ (a), $Zn_{0.95}Co_{0.05}O$ (b), and $Zn_{0.97}Cu_{0.03}O$ (c) thin films at 300 K (Fig. 12). The curve shows the room-temperature ferromagnetism for the entire TM-doped ZnO thin films [18–20]. The saturation magnetic moment of $Zn_{0.95}Co_{0.05}O$ thin film is 0.42 μ_B/Co atom. Similarly, $Zn_{0.97}Ni_{0.03}O$ and $Zn_{0.97}Cu_{0.03}O$ thin films show saturation magnetization of 0.28 μ_B/Ni atom and 0.24 μ_B/Cu atoms, respectively. But the pristine ZnO thin films grown by PLD show diamagnetic nature. The shape of the curve reveals that there is some trace of paramagnetism in $Zn_{0.95}Co_{0.05}O$ thin film also. According to Ruderman–Kittel–Kasuya–Yoshida (RKKY) theory, the magnetism is due to the exchange interaction between local spin-polarized electrons and conduction electrons. The spin polarization of the conduction electrons in ZnO films performs an exchange interaction with spin-polarized electrons of other TM ions. The magnetization increases in the films, when the oxygen partial pressure during the deposition of the films decreases, due to the formation of defects or increased carrier concentrations [6, 9, 35, 41, 68, 73–75, 83, 115, 117, 120, 135, 136]. $Zn_{0.97}TM_{0.03}O$ thin films prepared at 450 °C and 0.05 mbar oxygen pressure show lower saturation magnetization than one prepared at 5×10^{-4} mbar pressure. Higher oxygen pressure results in less oxygen vacancies

and reduces the carrier concentration. This supports the assumption that magnetism is due to the exchange interaction between local spin-polarized electrons and conduction electrons. At higher concentrations, the TM clusters and transition-metal oxides suppress the room-temperature ferromagnetism in $Zn_{1-x}TM_xO$ thin films and paramagnetism is observed [6, 35, 73, 74, 83, 92, 115]. X-ray diffraction pattern, Raman spectra, and XPS measurements overruled the formation of secondary phases in $Zn_{1-x}TM_xO$ films within the experimental detection limit.

5.4 Growth of ZnO:TM Nanostructures by Hydrothermal Technique

ZnO nanoparticles can be prepared on a large scale by low-cost simple solution-based methods, such as chemical precipitation [137, 138], sol-gel synthesis [139], and solvothermal/hydrothermal reaction [140–142]. The advantages of low-cost hydrothermal process are catalyst-free growth, large area production, and eco-friendly. The existence of RTFM in Cu-/Ni-/Mn-doped ZnO is visualized by various groups [6, 35, 73–75, 83, 120, 143–146]. But the origin of ferromagnetism is still debatable whether it is due to the formation of impurity phases or clusters during the growth process [6, 41, 68, 115, 147]. The hydrothermal synthesis of ZnO and ZnO:TM nanostructures and the effect of TM concentration on the structural, optical, morphological, and magnetic properties have been reported from our laboratory [148, 149].

(a) **Growth parameters**

Pristine ZnO and ZnO:TM nanostructures were grown by hydrothermal method. An appropriate amount of ammonium hydroxide was added to the mixture of zinc acetate (0.3–1 M) and copper acetate or nickel acetate or manganese acetate (0.001–0.1 M) solution to maintain the pH value around 11. ZnO:TM nanostructures were synthesized hydrothermally at 150 °C for 3 h by keeping the concentration of $Zn(CH_3COO)_2$ as 1 M in all reactions, while the concentration of $TM(CH_3COO)_2$ was varied from 0.001 M to 0.1 M. The molarity of TM in nanostructures is varied by adjusting the concentrations of zinc acetate and TM acetate precursors. After the reaction was complete, the resulting solid products were washed with methanol, filtered, and then dried in air in a laboratory oven at 60 °C.

(b) **Characterizations**

Phase purity of hydrothermally grown pristine and TM-doped ZnO shows wurtzite phase without any impurity phases within the experimental detection limit. All samples show diffraction pattern match with the reported ICSD data [150]. SEM images of pristine ZnO- and TM-doped ZnO nanostructures prepared using 0.05 M $TM(CH_3COO)_2$ in the precursor solution at 150 °C for 6 h are shown in Fig. 13. SEM images confirm the formation of ZnO nanostructures and are assembled like
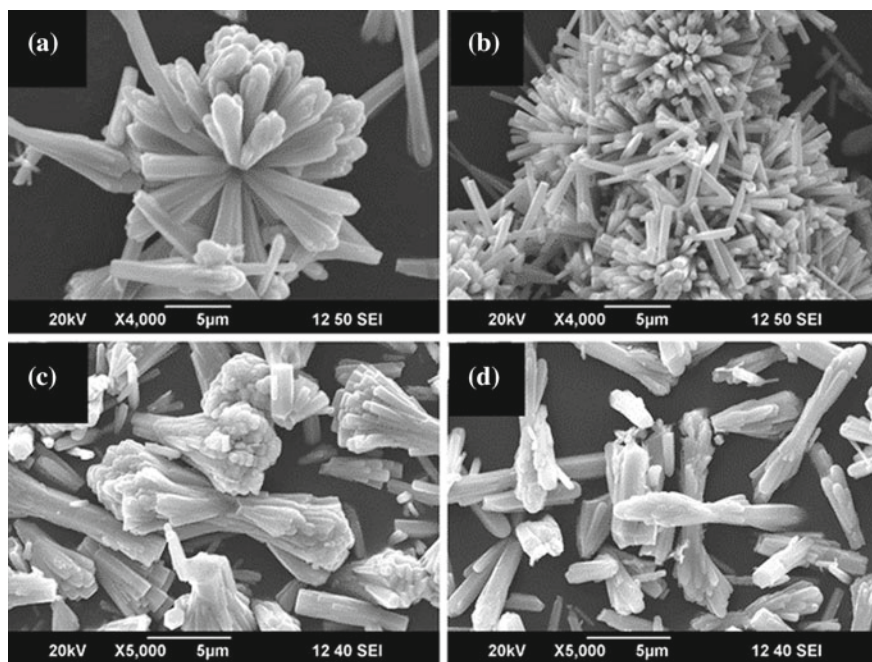
Fig. 13 SEM images of pristine ZnO and ZnO:TM nanostructures synthesized at 150 °C for 6 h **a** pristine ZnO and ZnO doped with 0.05 M, **b** Cu(CH₃COO)₂, **c** Mn(CH₃COO)₂, **d** Ni(CH₃COO)₂ in the precursor solution

branched structures. The 'TM' doping changes the morphology, and we get uniformly elongated nanorods in the form of bunches.

The band gap of ZnO:TM nanostructures shows red shift with increase of TM doping. The red shift shown by transition-metal-doped II–VI semiconductors is due to 's-d' and 'p-d' exchange interactions between the band electrons of the host lattice and localized d-electrons of substituted magnetic impurities. Diouri et al. [151] and Bylsma et al. [152] had theoretically explained the mechanism behind 's-d' and 'p-d' exchange interactions using second-order perturbation theory attributed to band gap narrowing. The red shift of the band gap confirms the substitution of TM into the ZnO lattice, and the band gap narrowing is due to the exchange interactions [152–154]. Figure 14 shows the photoluminescence spectra of ZnO:TM nanostructures ($\lambda_{exc} = 325$ nm). ZnO:Cu nanostructures have two emission bands, an ultraviolet (UV) emission band at 370 nm and a broad orange-red emission centered at 630 nm [155]. Other TM (Mn/Ni)-doped ZnO nanostructures have PL spectra similar to pristine ZnO nanostructures. But the UV emission is attributed to the near-band-edge free-exciton transition [156]. Green and yellow emissions are the most commonly observed defect emissions in ZnO nanostructures [157, 158]. The green emission is attributed to oxygen vacancies or zinc interstitials [159]. Yellow defect emission is

Fig. 14 Room-temperature PL spectra ($\lambda_{exc}= 325$ nm) of ZnO:TM nanostructures synthesized at 150 °C for 3 h with 0.05 M TM concentration
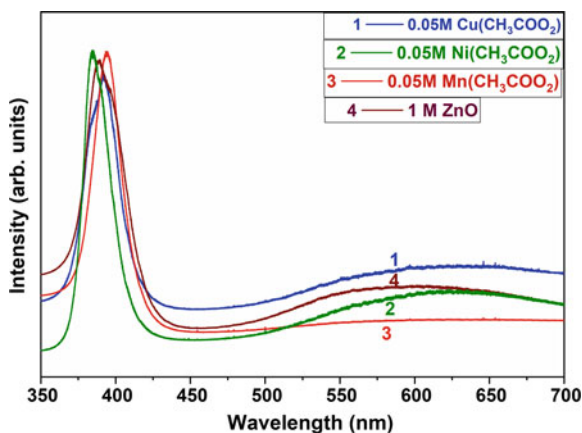
typically attributed to oxygen interstitials [160]. The intensity of the green–yellow-related emission due to defect was found to be dependent also on the nanowire diameter [157]. Cu impurities have been proposed as origin of the green emission in Cu-doped ZnO materials [161]. According to Fan et al. [162], ZnO dendritic wires and nanosheets show visible emission components centered at ~540 and ~610 nm.

Characteristics of Raman modes E^2_{low}(100 cm^{-1}), second phonon line-2 E^M_2(332 cm^{-1}), A^{TO}_1(380 cm^{-1}), E^2_{high} (437 cm^{-1}), and A^{LO}_1(580 cm^{-1}) of TM-doped ZnO nanostructures are shown in Fig. 15. The slight broadening of the E^2_{high} modes and its red shift from the bulk value indicates the substitution of TM ions into the ZnO sublattice [126–134]. Structural disorders, crystal defects, and enhanced residual stress are responsible for the observed peak broadening and mode shifts in TM-doped ZnO nanostructures.

The field-dependent magnetization curve of ZnO:TM (TM = Cu, Mn, Ni) nanostructures at 300 K is shown in Fig. 16. The noticeable coercivity of M-H loops

Fig. 15 Raman spectra of ZnO:TM nanostructures synthesized at 150 °C for 3 h with 0.05 M TM concentration
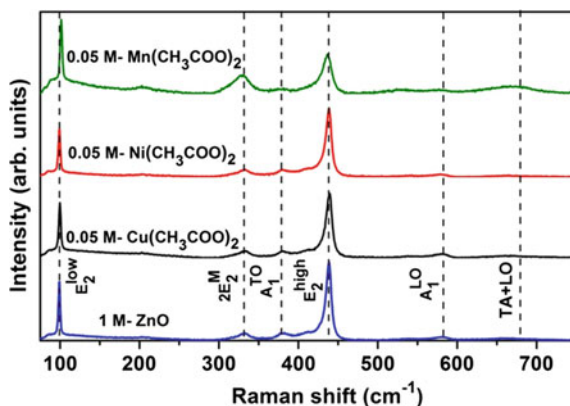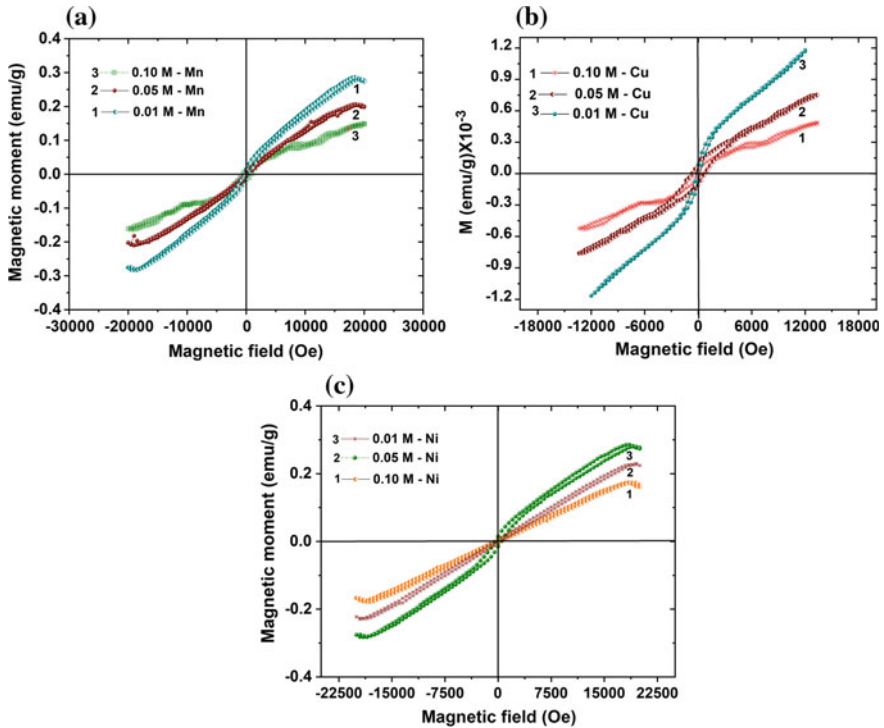
Fig. 16 Room-temperature M-H loop of ZnO:TM nanostructures with various concentrations of TM doping

could be attributed to strong ferromagnetism at room temperature. The ferromagnetic behavior of nanostructures imputed to the presence of small magnetic dipoles located at the surface of nanostructures. So the nearest-neighbor interactions can make the magnetic dipoles of neighboring dipoles oriented along the direction of the applied magnetic field. Surface-to-volume ratio is large for nanostructures; as a result, the population of oriented magnetic dipoles will increase at the surface. At higher TM doping concentrations enhanced antiferromagnetic interaction between neighboring TM-TM ions suppress the ferromagnetism. The hysteresis loop of ZnO:TM nanostructures was not saturated, so we one can expect some traces of paramagnetism. Origin of magnetism in DMSs is still controversial; the most common mechanism for observed ferromagnetism in ZnO:TM nanostructures is the carrier-induced ferromagnetism (RKKY mechanism), often reported for DMSs [6, 35, 68, 74, 83, 92, 149]. Secondary phases or clusters are even responsible for the observed magnetic nature. The broadening and the shift of (97) peaks in the XRD pattern confirm the incorporation of TM ions into the ZnO lattice X-ray diffraction, and Raman spectra analysis could not find any cluster or secondary phase formation in ZnO:TM nanostructures.

5.5 *Origin of Ferromagnetism in ZnO-Based DMSs*

Before elucidating the mechanisms of intrinsic RTFM, it must first be confirmed whether the magnetic hysteresis loops measured are intrinsic or extrinsic. Magnetic contamination [68], measurement errors [78, 79], and secondary phases [6, 68, 92] are all possibilities for FM signals. Both metals and their oxides have been identified as being responsible for FM behavior in TM-doped ZnO films, such as Co [6, 41, 68], Mn [6, 163], CoFe [6], CoO [6, 68], Co_3O_4 [6, 68, 92, 115], Fe_3O_4 [6], and CuO [6]. These types of TM-doped ZnO films are not genuine DMS. However, these non-magnetic semiconductors with embedded secondary FM phases may exhibit an anomalous Hall effect (AHE) [6], which was previously considered an indicator of whether a doped sample was a DMO or not. AHE was observed in FM ZnO and in non-FM Cu-doped ZnO films, indicating that AHE does not uniquely demonstrate FM behavior [6, 164]. Therefore, checking for basic experimental reproducibility, in addition to carrying out careful characterizations, is highly warranted.

(a) **Co-doped ZnO**

It has been examined that ferromagnetic interactions may originate from Co_3O_4 like secondary phases in ZnCoO system [165]. Sharma et al. [166] reported the carriers mediated mechanism in Co-doped ZnO-based DMS material. 'Double exchange' [167] and 'mean field Zener model' [168] have also been reported as the possible mechanisms for ferromagnetism in this composition. In addition, it was also detected that ferromagnetism in this system might arise because of simple substitution of 'Co' at Zn sites [169] or oxygen vacancies [170]. More recently, Zhang [169] expected that Al substitution played a crucial role to achieve the ferromagnetic behavior through first principle calculations. Hence, the origin of RT ferromagnetic interactions in ZnO-based DMSs has remained controversial among research community and still required further studies for its clarification. The controversies among researchers suggest that ferromagnetic behavior and its origin in DMSs depend on composition, synthesis conditions, annealing parameters, and additional dopants for varying the concentration of carriers as well. Moreover, origin of room temperature ferromagnetism can only be clarified when prepared materials will be free from any impurity or secondary phases. So we need to synthesize phase pure DMSs to explore its magnetic properties and mechanisms.

(b) **Mn-doped ZnO**

It has been observed that ferromagnetic behavior in ZnO:Mn materials may originate from the Mn_3O_4 like secondary phases [163]. But recently, Yang and co-workers [171] observed that origin of room temperature ferromagnetic interactions could not be derived from any secondary or impurity phase. Mn substitution at Zn sites in ZnO structure might be the main reason for existence of this ferromagnetism. According to the RKKY theory [172], this ferromagnetism arises from the magnetic exchange interactions between conduction electrons and local spin-polarized electrons (for instance, the electrons of Mn^{2+}). Free charge carriers, i.e., electrons, play crucial role

in establishment of magnetic phase and consequently the ferromagnetic behavior in magnetic element-doped ZnO [173–175].

(c) **Ni-doped ZnO**

According to RKKY theory [176], the presence of exchange interactions among conduction electrons and local spin-polarized carriers (as electrons of Ni^{2+} ions) is the main reason of ferromagnetism in DMS materials. Secondary phases or interactions among two magnetic atoms like Ni-Ni [177] might also be responsible for ferromagnetism. Moreover, vacancy [178] and carrier's induced magnetism [179–181] have also been reported for Ni-doped ZnO. On the other hand, it was also observed that ferromagnetism in these materials was independent of carrier concentration.

(d) **Magnetic behavior of pure ZnO**

Transition-metal-doped ZnO is one of the most studied systems due to its predicted ferromagnetic transition temperature above room temperature [5, 15]. However, the experimental findings from different groups are sometimes vastly contradictory. While many groups report room temperature ferromagnetism of Co-doped ZnO [6, 41, 68, 83, 92], there are many other groups reporting the absence of ferromagnetism or suppression of RTFM with Co-doping [6, 10–12, 115]. This suggests that the properties of these materials are highly process-dependent and the origins of ferromagnetism in these materials are still under debate. It has been shown very recently that intrinsic ferromagnetism is observed in pure TiO_2 and ZnO thin films and nanostructures. There is a lot of discussion going on about the extrinsic and the intrinsic origins of ferromagnetism in TM-doped oxide semiconductors. Using magnetic measurements and magnetotransport studies, Sayak et al. [115] showed that the doping with transition metal is not a prerequisite for observing magnetic moments in ZnO thin films. Also they emphasize the fact that the doping of the transition metal in the ZnO matrix in fact lowers the magnetic moment of the pure ZnO film [92]. They tuned the intrinsic magnetic moment in pure ZnO film by appropriate oxygenation. In the magnetoresistance data for the undoped film, a clear change of sign is observed, which clearly indicates that there is change in the intrinsic property of the sample between before and after the oxygen treatment. Again magnetotransport results support the magnetization data which suggest that pristine ZnO is a better candidate for room-temperature semiconductor spintronic devices than Co-doped ZnO.

6 Summary

Dilute magnetic semiconductors are useful materials for future spintronic applications due to semiconducting host lattice and half-metallicity. But most of DMS shows low Curie temperatures. In this article, we have discussed the origin of ferromagnetism and correlated it with ab initio calculations for the electronic and magnetic properties of transition-metal-doped ZnO semiconductors. Most of the results point

of the existence of DMS with different magnetic interactions. In systems with localized majority d-states deep in the valence band, the ferromagnetism is induced by Zener's p-d exchange interaction, leading to holes in the majority p-valence band. At higher TM concentrations, the Curie temperature is reduced due to enhanced antiferromagnetic interactions via superexchange interactions. In systems with impurity bands in the band gap (heavily doped systems), the ferromagnetism is driven by Zener's double-exchange, magnetic polarons, or RKKY interactions. Here the magnetic coupling is strong, but it is short-ranged. A way to achieve higher Curie temperatures might be to try to increase the impurity concentration without forming secondary or binary compounds. Recently, A. Tiwari's groups have realized a prototype spintronic device [182]. A lot of groups have produced contradictory results, and all these lead to the conclusion that the realization of the spintronic device needed a careful preparation and device formation technique. The future of spintronic device is really big, so the technological revolution will be unfolded to mankind in a few decades (Table 1).

Table 1 Summary of method of synthesis and properties of selected DMS

Obtained morphology	Fabrication method	Magnetic state	Magnetization	Proposed theories	References
Nanoparticles	Forced hydrolysis	Weak RTFM	0.2 to ~1.5 memu/g	Zn interstitials and O vacancies induced by annealing enhanced magnetization	[183]
Nanopowder	Mechanical milling and annealing	RTFM	3 memu/g	Zn vacancies at grain surface	[184]
Nanoparticles	Mechanical milling	RTFM		Zinc vacancies	[185]
Nanorods	Chemical vapor deposition (high temperature)	RTFM	0.031 emu/g	Single-ionized oxygen vacancies for BMPs (EPR and PL analysis)	[186]
	Chemical bath deposition (low temperature)		0.06 emu/g		
Nanoparticle pellet	Annealing in oxygen	Diamagnetism	–	Zn vacancy + OH bonding complex results in a net magnetization	[187]
	Annealing in hydrogen	Weak RTFM	0.7 emu/g		

(continued)

Table 1 (continued)

Obtained morphology	Fabrication method	Magnetic state	Magnetization	Proposed theories	References
Nanoparticle	Solution route and annealing in N_2, Ar, and O_2	RTFM	1.5 memu/g	Singly ionized oxygen vacancies	[188]
Nanowire	Vapor transport	RTFM	0.0076 μ_B / V_o	Oxygen vacancies	[185]
Nanowire	Hydrothermal and annealing in air and O_2	RTFM	1 memu/g	Singly ionized oxygen vacancies	[189]
Nanorod	Wet chemical	RTFM	1.5 memu/g	Size effect; singly ionized oxygen vacancies	[190]
Nanoparticles	Wet chemical method	RTFM	1.5 memu/g	Singly ionized oxygen vacancies	[182]
Nanorod array	Hydrothermal and annealing in H_2 and O_2	RTFM	0.15 emu/g	Oxygen vacancies	[191]
Nanowire	Chemical vapor deposition	Weak RTFM	0.2 memu/g	Surface defects and dynamic exchange between O_2 and O_2	[192]
	Pulsed laser vaporization	Diamagnetism	–		
Nanoparticles and nanorods	Chemical method	RETM with super paramagnetism	1.75 emu/g	Inhomogeneities created due to NPs	[193]

References

1. Service RF (1997) Science 276:895
2. Bangall DM, Chen YF (1997) Appl Phys Lett 70:2230
3. Chen YF, Bangall DM (1997) J Appl Phys 84:3912
4. Djurisic AB, Leung YH (2006) Small 2:944
5. Ohno H (1998) Science 281:951
6. Pan F, Song C, Liu XJ, Yang YC, Zeng F (2008) Mater Sci Eng Res 62:1–35
7. Singh S, Thiyagarajan P, Kant KM, Anita D, Thirupathiah S, Rama N, Tiwari B, Kottaisamy M, Rao MSR (2007) J Phys D Appl Phys 40:6312–6327
8. Ozgur U, Alivov YI, Liu C, Teke A, Reshchikov MA, Dogan S, Avrutin V, Cho SJ, Morko H (2005) J Appl Phys 98:041301
9. Pearton SJ, Heo WH, Ivill M, Norton DP, Steiner T (2004) Semicond Sci Technol 19:R59–R74
10. Tanaka M (1998) J Vac Sci Technol, B 16:2267
11. Ohtomo A, Kawasaki M, Koida T, Masubuchi K, Koinuma H, Sakurai Y, Yoshida Y, Segawa Y (1998) Appl Phys Lett 72:2466
12. Matsukura F, Ohno H, Schen A, Sugawara Y (1998) Phys Rev B 57:R2037

13. Morkoc H, Ozgur U (2009) Zinc oxide fundamentals, materials and device technology. Wiley-VCH Verlag GmbH & Co. KGaA, Weinheim
14. Wolf SA, Awschalom DD, Buhrman RA, Daughton JM, von Molnar S, Roukes ML, Chtchelkanova AY, Treger DM (2001) Science 294:1488
15. Dietl T, Ohno H, Matsukura F (2000) Science 287:1019
16. Sarma SD (2001) Am Sci 89:516
17. King SL, Gardeniers JGE, Boyd IW (1996) Appl Surf Sci 96:811
18. Gao PX, Lao CS, Hughes WL, Wang ZL (2005) Chem Phys Lett 408:174
19. Yang HY, Lau SP, Yu SF, Abiyasa AP, Tanemura M, Okita T, Hatano H (2006) Appl Phys Lett 89:011103–11111
20. Li C, Fang G, Su F, Li G, Wu X, Zhao X (2006) Nanotechnology 17:3740
21. Arun Aravind A, Jayaraj MK, Kumar M, Chandra R (2013) Appl Surf Sci 286:54–60
22. Blundell S (2001) Magnetism in condensed matter. Oxford University Press, New York
23. Coey JMD, Venkatesan M, Fitzgerald CB (2005) Nat Mater 4:173
24. Dietl T, Spalek JJ (1983) Phys Rev B 28:1548–1563
25. Angelescu DE, Bhatt RN (2002) Phys Rev B 65:075211
26. Durst AC, Bhatt RN, Wolff PA (2002) Phys Rev B 65:235205
27. Matsumoto Y, Murakami M, Shono T, Hasegawa T, Fukumura T, Kawasaki M, Ahmet P, Chikyow T, Koshihara SY, Koinuma H (2001) Science 291:854
28. Chambers SA, Thevuthasan S, Farrow RFC, Marks RF, Thiele JU, Folks L, Samant MG, Kellock AJ, Ruzycki N, Ederer DL, Diebold U (2001) Appl Phys Lett 79:3467
29. Stampe PA, Kennedy RJ, Yan X, Parker JS (2002) J Appl Phys 92:7114
30. Kim JY, Park JH, Park B-G, Noh HJ, Oh SJ, Yang JS, Kim DH, Bu SD, Noh TW, Lin HJ, Hsieh HH, Chen CT (2003) Phys Rev Lett 90:017401-
31. Kimura H, Fukumura T, Kawasaki M, Inaba K, Hasegawa T, Koinuma H (2002) Appl Phys Lett 80:94
32. Ogale SB, Choudhary RJ, Buban JP, Lofland SE, Shinde SR, Kale SN, Kulkarni VN, Higgins J, Lanci C, Simpson JR, Browning ND, Das Sarma S, Drew HD, Greene RL, Venkatesan T (2003) Phys Rev Lett 91:077205
33. Sato K, Yoshida HK (2001) Jpn J Appl Phys 40:L334
34. Yoshida HK, Sato K (2003) Phys B 327:337
35. Sharma P, Gupta A, Rao KV, Owens FJ, Sharma R, Ahuja R, Guillen JMO, Johansson B, Gehring GA (2003) Nature Mater 2:673
36. Fukumura T, Kawasak M (2001) Appl Phys Lett 78:958
37. Kim SS, Moon JH, Lee BT, Song OS, Je JH (2004) J Appl Phys 95:454
38. Pradha K, Zhang K, Mohanty S (2005) Appl Phys Lett 86:152511
39. Chang YQ, Wang DB, Luo XH (2002) Appl Phys Lett 83:4020
40. Fukumura T, Jin C, Ohtomo A, Koinuma H, Kawasaki M (1999) Appl Phys Lett 75:3366
41. Ueda K, Tabata H, Kawai T (2001) Appl Phys J Appl Phys 39:988
42. Kim JH, Kim H, Kim D, Ihm YE, Choo WK (2002) J Appl Phys 92:6066
43. Chakraborti D, Narayan J, Prater JT (2007) Appl Phys Lett 90:062504
44. Jin Z, Fukumura T, Kawasaki M, Ando K, Saito H, Yoo YZ, Murakami M, Matsumoto Y, Hasegawa T, Koinuma H (2001) Appl Phys Lett 78:3824
45. Buchholz DB, Chang RPH, Song JH, Ketterson JB (2005) Appl Phys Lett 87:082504
46. Ye JD, Gu SL, Qin F, Zhu SM, Liu SM, Zhou X, Liu W, Hu LQ, Zhang R, Shi Y, Zheng YD, Ye YD (2005) Appl Phys A 81:809
47. Mao X, Zhong W, Du Y (2008) J Magn Magn Mater 320:1102
48. Bodker F, Hansen MF (2000) J Magn Magn Mater 221:32
49. Yin Z, Chen N (2005) J Magn Magn Mater 135:430
50. Lu JJ, Lin TC, Tsai SY, Mo TS, Gan KJ (2011) J Magn Magn Mater 323:829
51. Ma L, Ma S, Chen H, Ai X, Huang X (2011) Appl Surf Sci 257:10036
52. Samanta K, Arora AK, Katiyar RS (2011) J Appl Phys 110:043523
53. Hu YM, Wang CY, Lee SS, Han TC, Chou WY, Chen GJ (2011) J Ramanspec 42:434
54. Li T, Qiu H, Wu P (2007) Thin Solid Films 515:3905

55. Baibich MN, Broto JM, Fert A, Nguyen Van Dau F, Petroff F, Etienne P, Creuzet G, Friederich A, Chazelas J (1988) Phys Rev Lett 61:2472
56. Parkin SS (1995) Gaint magnetoresistance in magnetic nanostructures. In: Wessels BW (ed) Annual review of materials science, vol 25. Annual Reviews Inc., Palo Alto, CA, p 357
57. Sato K, Yoshida HK (2001) Materials research society symposium proceedings, vol 666, F4.6.1
58. Ramachandran S, Prater JT, Sudhakar N, Kumaer D, Narayan J (2008) Solid State Commun 145:18
59. Dietl T, Ohno H, Matsukura F (2001) Phys Rev B 63:195205
60. Gacic M, Jakob G, Herbort C, Adrian H (2007) Phys Rev B 75:205206
61. Sato K, Yoshida HK (2000) Jpn J Appl Phys 39:L555
62. Akai H, Dederichs PH (1993) Phys Rev B 47:8739
63. Filippetti A, Spaldin NA (2003) Phys Rev B 67:125109
64. Yun SY, Cha GB, Kwon Y, Cho S, Hong SC (2004) J Magn Magn Mater 272–276:e1563–e1564
65. Toyoda M, Akai H, Sato K, Yoshida HK (2006) Phys B 376–377:647
66. Chien CH, Chiou SH, Guo GY, Yao YD (2004) J Magn Magn Mater 282:275–278
67. Pemmaraju CD, Archer T, Hanafin R, Sanvito S (2007) J Magn Magn Mater 316:e185
68. Ivill M, Pearton SJ, Rawal S, Leu L, Sadik P, Das R, Hebard AF, Chisholm M, Budai JD, Norton DP (2008) New J Phys 10:065002
69. Lee HJ, Jeong S-Y, Cho CR, Park CH (2002) Appl Phys Lett 81:18
70. Samanta K, Bhattacharya P, Katiyar RS (2006) Phys Rev B 73:245213
71. Prellier W, Fouchet A, Mercey B (2003) J Phys Condens Matter 15:R1583–R1601
72. Yang SG, Pakhomov AB, Hung ST, Wong CY (2002) IEEE Trans Magn 38:2877
73. Sharma P, Gupta A, Owens FJ, Inoue A, Rao KV (2004) J Magn Magn Mater 282:115
74. Aravind A, Jayaraj MK, Kumar M, Chandra R (2012) Mater Sci Eng B 177:1017
75. Ma JG, Liu YC, Mu R, Zhang JY, Lu YM, Shen DZ, Fan XW (2004) J Vac Sci Technol B 22:94
76. Alaria J, Bieber H, Colis S, Schmerber G, Dinia A (2006) Appl Phys Lett 88:112503
77. Chambers SA, Droubay TC, Wang CM, Rosso KM, Heald SM, Schwartz DA, Kittilstved KR, Gamelin DR (2006) Mater Today 9:28
78. Abraham DW, Frank MM, Guha S (2005) Appl Phys Lett 87:252502
79. Ney A, Kammermeier T, Ney V, Ollefs K, Ye S (2008) J Magn Magn Mater 320:3341–3346
80. Song C, Geng KW, Zeng F, Wang XB, Shen YX, Pan F, Xie YN, Liu T, Zhou HT, Fan Z (2006) Phys Rev B 73:024405
81. Janisch R, Gopal P, Spaldin NA (2005) J Phys Condens Matter 17:R657
82. Song C, Zeng F, Geng KW, Liu XJ, Pan F, He B, Yan WS (2007) Phys Rev B 76:045215
83. Aravind A, Hasna K, Jayaraj MK, Kumar M, Chandra R (2014) Appl Phys A 115:843
84. Herng TS, Lau SP, Yu SF, Chen JS, Teng KS (2004) J Magn Magn Mater 315:107
85. Lin YH, Ying M, Li M, Wang X, Nan CW (2007) Appl Phys Lett 90:222110
86. Khare N, Kappers MJ, Wei M, Blamire MG, Macmanus-Driscoll JL (2006) Adv Mater 18:1449
87. Zhang YB, Liu Q, Sritharan T, Gan CL, Li S (2006) Appl Phys Lett 89:042510
88. Herng TS, Lau SP, Yu SF, Yang HY, Ji XH, Chen JS, Yasui N, Inaba H (2006) J Appl Phys 99:086101
89. Tuan AC, Bryan JD, Pakhomov AB, Shutthanandan V, Thevuthasan S, McCready DE, Gaspar D, Engelhard MH, Rogers JW Jr, Krishnan K, Gamelin DR, Chambers SA (2004) Phys Rev B 70:054424
90. Dinia A, Schmerber G, Pierron-Bohnes V, Mény C, Panissod P, Beaurepaire E (2005) J Magn Magn Mater 286:37
91. Li XL, Wang ZL, Qin XF, Wu HS, Xu XH, Gehring GA (2008) J Appl Phys 103:023911
92. Ghoshal S, Anil Kumar PS (2008) J Magn Magn Mater 320:L93
93. Zheng Y, Boulliard JC, Demaille D, Bernard Y, Pétroff JF (2005) J Cryst Growth 274:156
94. Mandal SK, Das AK, Nath TK, Karmakar D (2006) Appl Phys Lett 89:144105

95. Nielsen K, Bauer S, Lubbe M, Goennenwein STB, Opel M, Simon J, Mader W, Gross R (2006) Phys Stat Sol A 203:3581
96. Sudakar C, Thakur JS, Lawes G, Naik R, Naik VM (2007) Phys Rev B 75:054423
97. Kioseoglou G, Hanbicki AT, Sullivan JM, van'TErve OMJ, Li CH, Erwin SC, Mallory B, Yasar M, Petrou A, Jonker BT (2004) Nat Mater 3:799
98. Liu XJ, Song C, Yang PY, Zeng F, Pan F (2008) Appl Surf Sci 254:3167
99. Park SY, Kim PJ, Lee YP, Shin SW, Kim TH, Kang JH (2007) Adv Mater 19:3496
100. Hsu HS, Huang JCA, Huang YH, Liao YF, Lin MZ, Lee CH, Lee JF, Chen SF, Lai LY, Liu CP (2006) Appl Phys Lett 88:242507
101. MacManus-Driscoll JL, Khare N, Liu Y, Vickers ME (2007) Adv Mat 19:2925
102. Lee S, Shon Y, Lee SW, Hwang SJ, Lee HS, Kang TW, Kim DY (2006) Appl Phys Lett 88:212513
103. Ramachandran S, Narayan J, Prater JT (2006) Appl Phys Lett 88:242503
104. Song C, Pan SN, Liu XJ, Li XW, Zeng F, Yan WS, He B, Pan F (2007) J Phys Condens Matter 19:176229
105. Liu XJ, Song C, Zeng F, Wang XB, Pan F (2007) J Phys D Appl Phys 40:1608
106. Schwartz DA, Gamelin DR (2004) Adv Mater 16:2115
107. Kittilsved KR, Schwartz DA, Tuan AC, Heald SM, Chambers SA, Gamelin DR (2006) Phys Rev Lett 97:037203
108. Chambers SA (2006) Surf Sci Rep 61:345
109. Kundaliya DC, Ogale SB, Lofland SE, Dhar S, Metting CJ, Shinde SR, Ma Z, Varughese B, Ramanujachary KV, Salamanca-riba L, Venkatesan T (2004) Nat Mater 3:709
110. Venkatesan M, Fitzgerald CB, Lunney JG, Coey JMD (2004) Phys Rev Lett 93:177206
111. Coey JMD, Douvalis AP, Fitzgerald CB, Venkatesan M (2004) Appl Phys Lett 84:1332
112. Liu H, Zhang X, Li L, Wang YX, Gao KH, Li ZQ, Zheng RK, Ringer SP, Zhang B, Zhang XX (2007) Appl Phys Lett 91:072511
113. Song C, Zeng F, Geng KW, Wang XB, Shen YX, Pan F (2007) J Magn Magn Mater 309:25
114. Behan AJ, Mokhtari A, Blythe HJ, Score D, Xu X-H, Neal JR, Fox AM, Gehring GA (2008) Phys Rev Lett 100:047206
115. Ghoshal S, Anil Kumar PS (2008) J Phys Condens Matter 20:192201
116. Norton DP, Pearton SJ, Hebard AF, Theodoropoulou N, Boatner LA, Wilson RG (2003) Appl Phys Lett 82:239
117. Ivill M, Pearton SJ, Norton DP, Kelly J, Hebard AF (2005) J Appl Phys 97:053904
118. Xu XH, Blythe HJ, Ziese M, Behan AJ, Neal JR, Mokhtari A, Ibrahim RM, Fox AM, Gehring GA (2006) New J. Phys. 8:135
119. Liu XJ, Song C, Zeng F, Pan F (2007) J Phys Condens Matter 19:296208
120. Tiwari A, Snure M, Kumar D, Abiade JT (2008) Appl Phys Lett 92:062509
121. Han SJ, Song JW, Yang CH, Park SH, Park JH, Jeong YH, Rhie KW (2002) Appl Phys Lett 81:4212
122. Hong NH, Brize V, Sakai J (2005) Appl Phys Lett 86:082505
123. Jayakumar OD, Gopalakrishnan IK, Kulshreshtha SK (2006) Adv Mater 18:1857
124. Yan W, Sun Z, Liu Q, Li Z, Shi T, Wang F, Qi Z, Zhang G, Wei S, Zhang H, Chen Z (2007) Appl Phys Lett 90:242509
125. Kim KJ, Park YR (2001) Appl Phys Lett 81:1420
126. Scott JF (1970) Phys Rev B 2:1209
127. Porto SPS, Krishnan RS (1967) J Chem Phys 47:1009
128. Ricchter H, Wang ZP, Ley L (1981) Solid State Commun 39:625
129. Ko HJ, Chen YF, Zhu Z, Hanada T, Yao T (2000) J Cryst Growth 208:389
130. Arnold MS, Avouris P, Pan ZW, Wang ZL (2003) J Phys Chem B 107:6599
131. Manjon FJ, Mari B, Serrano J, Romero AH (2005) J Appl Phys 97:053516
132. Wang XB, Song C, Geng KW, Zeng F, Pan F (2007) Appl Surf Sci 253:6905
133. Hu YM, Wang CY, Lee SS, Han TC, Chou WY (2010) Thin Solid Films 519:1272
134. Hu YM, Wang CY, Lee SS, Han TC, Choub WY, Chen GJ, Raman J (2011) Spectroscopy 42:434

135. Kodama RH, Makhlouf SA, Berkowitz AE (1997) Phys Rev Lett 79:1393
136. Calderon MJ, Sarma SD (2007) Annals Phys 322:2618
137. Zhong QP, Matijevic E (1996) J Mater Chem 3:443
138. Lingna W, Mamoun M (1999) J Mater Chem 9:2871
139. Bahnemann DW, Kormann C, Hoffmann MR (1987) J Phys Chem 91:3789
140. Hui Z, Deren Y, Xiangyang M, Yujie J, Jin X, Duanlin Q (2004) Nanotechnology 15:622
141. Zhang J, Sun LD, Yin JL, Su HL, Liao CS, Yan CH (2002) J Mater Sci Lett 14:4172
142. Li WJ, Shi EW, Zheng YQ, Yin ZW (2001) J Mater Sci Lett 20:1381
143. Lee CY, Tseng TY, Li SY, Lin P (2006) J Appl Phys 99:024303
144. Guo S, Du Z, Dai S (2009) Phys Stat Sol B 246:2329
145. Cheng ZX, Wang XL, Dou SX, Ozawa K, Kimura H, Munroe P (2007) J Phys D Appl Phys 40:6518
146. Ankiewicz AO, Gehlhoff W, Martins JS, Pereira S, Pereira S, Hoffmann A, Kaidashev EM, Rahm A, Lorenz M, Grundmann M, Carmo MC, Trindade T, Sobolev NA (2009) Phys Stat Sol B 246:766
147. Andriotis AN, Menon M (2011) Phys Stat Sol B 248:2032
148. Aneesh PM, Cherian CT, Jayaraj MK, Endo T (2010) J Ceramic Soc Jpn 118:333
149. Aravind A, Jayaraj MK, Kumar M, Chandra R (2012) J Mater Sci Mater Electron 24:106–112
150. ICSD. Number 086254
151. Diouri J, Lascaray JP, El Amrani M (1985) Phys Rev B 31:7995
152. Bylsma RB, Becker WM, Kossut J, Debska U (1986) Phys Rev B 33:8207
153. Gamelin DR (2002) J Am Chem Soc 124:15192
154. Radovanovic PV, Gamelin DR (2003) Phys Rev Lett 91:157202
155. Dai L, Chen XL, Wang WJ, Zhou T, Hu BQ (2003) J Phys Condens Matter 15:2221
156. Wang H, Wang HB, Yang FJ, Chen Y, Zhang C, Yang CP, Li Q, Wong SP (2006) Nanotechnology 17:4312
157. Huang MH, Mao S, Feick H, Yan H, Wu Y, Kind H, Weber E, Russo R, Yang P (2001) Science 292:1897
158. Meng XQ, Shen DZ, Zhang JY, Zhao DX, Lu YM, Dong L, Zhang ZZ, Liu YC, Fan XW (2005) Solid State Commun 135:179
159. Liu X, Wu X, Cao H, Chang RPH (2004) J Appl Phys 95:3141
160. Greene LE, Law M, Goldberger J, Kim F, Johnson JC, Zhang Y, Saykally RJ, Yang P (2003) Angew Chem 115:3030
161. Garces NY, Wang L, Bai L, Giles NC, Halliburton LE, Cantwell G (2002) Appl Phys Lett 81:622
162. Fan HJ, Scholz R, Kolb FM, Zacharias M (2004) Appl Phys Lett 85:4142
163. Wang HB, Wang H, Zhang C, Yang FJ, Yang CP, Gu HS, Zhou MJ, Li Q, Jiang Y (2009) Mater Chem Phys 113:884
164. Prestgard MC, Tiwari A (2014) Appl Phys Lett 104:122402
165. Zhou X, Ge S, Yao D, Zuo Y, Xia Y (2008) Phys B 403:3336
166. Sharma VK, Xalxo R, Varma GD (2007) Crys. Res. Tech. 42:34
167. Li BB, Shen HL, Zhang R, Xiu XQ, Xie Z (2007) Chin Phys Lett 24:3473
168. Yang JH, Zhao LY, Ding X, Yang LL, Zhang YJ, Wang YX, Liu HL (2009) Mater Sci Eng B 162:143
169. Zhang XM, Mai W, Zhang Y, Ding Y, Wang ZL (2009) Solid State Commun 149:293
170. Singhal RK, Arvind S, Xing YT, Sudhish K, Dolia SN, Deshpande UP, Shripathiand T, Saitovitch EB (2010) J All Comp 496:324
171. Yang T, Li Y, Zhu MY, Li YB, Huang J, Jin HM, Hu YM (2010) Mater Sci Eng B 170:129
172. Sharma VK, Xalxo R, Varma GD (2007) Cryst Res Tech 42:34
173. Singh S, Rama N, Rao R (2006) Appl Phys Lett 88:222111
174. Kittilstved KR, Norberg NS, Gamelin DR (2005) Phys Rev Lett 94:147209
175. Kittlstved KR, Liu WK, Gamelin DR (2006) Nat Mater 5:291
176. Tong LN, He XM, Han HB, Hu JL, Xia AL, Tong Y (2010) Sol Stat Comm 150:1112
177. Huang GJ, Wang JB, Zhong XL, Zhou GC, Yan HL (2007) J Mater Sci 42:6464

178. Yu Z, Ge S, Zuo Y, Wang G, Zhang F (2010) Appl Surf Sci 256:5813
179. Pei G, Xia C, Cao S, Zhang J, Wu F, Xu J (2006) J Magn Magn Mater 302:340
180. Cheng C, Xu G, Zhang H, Luo Y (2008) Mater Lett 62:1617
181. Xu Q, Schmidt H, Zhou S, Potzger K, Helm M, Hochmuth H, Lorenz M, Setzer A, Esquinazi P, Meinecke C, Grundmann M (2008) Appl Phys Lett 92:082508
182. Xu X, Xu C, Dai J, Hu J, Li F, Zhang S (2013) J Phys Chem C 116:8813
183. Rainey K, Chess J, Eixenberger J, Tenne DA, Hanna CB, Punnoose A (2014) J Appl Phys 115:17D727
184. Ghose S, Sarkar A, Chattopadhyay S, Chakrabarti M, Das D, Rakshit T, Ray SK, Jana D (2013) J Appl Phys 114:073516
185. Phan TL, Zhang YD, Yang DS, Nghia NX, Thanh TD, Yu SC (2013) Appl Phys Lett 102:072408
186. Xu X, Xu C, Lin Y, Li J, Hu J (2013) J Phys Chem C 117:24549
187. Xue X, Liu L, Wang Z, Wu Y (2014) J Appl Phys 115:033902
188. Liu W, Li W, Hu Z, Tang Z, Tang X (2011) J Appl Phys 110:013901
189. Xing GZ, Wang DD, Yi JB, Yang LL, Gao M, He M, Yang JH, Ding J, Sum TC, Wu T (2010) Appl Phys Lett 96:112511
190. Podila R, Queen W, Nath A, Arantes JT, Schoenhalz AL, Fazzio A, Dalpian GM, He J, Hwu SJ, Skove MJ (2010) Nano Lett 10:1383
191. Kushwaha A, Tyagi H, Aslam M (2013) AIP Adv 3:042110
192. Xu X, Xu C, Lin Y, Ding T, Fang S, Shi Z, Xia W (2012) J Appl Phys Lett 100:172401
193. Chanda A, Gupta S, Vasundhara M, Joshi SR, Muttae GR, Singh J (2017) RSC Adv 7:50527